THE ASTROPHYSICAL JOURNAL, 433:48–64, 1994 September 20

THE NUCLEAR SUPERBUBBLE OF NGC 3079

S. VEILLEUX,[1,2,3] G. CECIL,[4] J. BLAND-HAWTHORN,[5] R. B. TULLY,[1]
A. V. FILIPPENKO,[6,7] AND W. L. W. SARGENT[8]
Received 1993 September 15; accepted 1994 March 23

ABSTRACT

We have used the Hawaii Imaging Fabry-Perot Interferometer (HIFI) at the CFH 3.6 m telescope to map Hα + [N II] λλ6548, 6583 emission-line profiles across the entire edge-on, nearby SBc galaxy NGC 3079, with resolution 70 km s^{-1} and subarsecond sampling. Blue and red long-slit spectra were obtained with the Double Spectrograph on the Palomar 5 meter telescope to provide additional emission-line diagnostics. A spectacular, line emitting bubble of diameter 13″ (∼1.1 kpc) is observed immediately east of the nucleus. Its unusual gaseous excitation (e.g., [N II] λ6583/Hα > 1) suggests that shocks are important. Extremely violent gas motions that range over 2000 km s^{-1} are detected across the bubble and diametrically opposite on the west side of the nucleus. Nonrotational motions are also found in the inner galaxy disk.

The complete spatial and spectral sampling of the emission-line profiles allows us to constrain the general flow pattern of the gas in the line-emitting bubble. An ovoidal bubble, inflated from the nucleus with monotonically increasing velocities ($V \propto R^n$ with $2 < n < 3$) and inclined ∼3° from the plane of the sky, provides a good first-order fit to its velocity field. A total ionized mass and kinetic energy of $\sim 1 \times 10^7/N_e\ M_\odot$ and $\sim 2 \times 10^{56}/N_e$ ergs, respectively, are involved in this outflow. Although the [S II] density in the bubble is only weakly constrained, we find no convincing evidence anywhere in the bubble (even near the nucleus) for the [S II] density to be above the low-density limit ($N_e \approx 125$ cm^{-3}). The radial density gradient previously reported in this galaxy is not confirmed, so the [S II] density profile cannot be used to find the size of the energy injection zone in this object. The Balmer decrements in the nucleus and the brighter regions of the outflow show a steep decrease in reddening away from the galaxy plane. The outflow mass is similar to, but the kinetic energy may be 10 times larger than, the superwinds in the Seyfert galaxy NGC 1068 and the starburst galaxy M82. Therefore, the superbubble of NGC 3079 is the most powerful example known of a wind-blown bubble, and an excellent laboratory to study wind dynamics. The dimensions and energies of the bubble imply that it is likely to be in the blowout phase and partially ruptured. The predicted rate of kinetic energy output from the central starburst appears sufficient to power most of this outflow. It is possible that a central active galactic nucleus also contributes to the outflow.

Subject headings: galaxies: individual (NGC 3079) — galaxies: kinematics and dynamics — galaxies: Seyfert — galaxies: structure — ISM: bubbles

1. INTRODUCTION

The interstellar medium (ISM) in our own Galaxy has been described as a "cosmic bubble bath" (Brand & Zealey 1975). Shells, arcs, bubbles, and cavities that result from strong localized deposition of energy from supernovae and stellar winds are superimposed on the large-scale gas distribution. Similar loops are found in the Magellanic Clouds, M31, M33, and other nearby late-type galaxies (cf. review by Tenorio-Tagle & Bodenheimer 1988). The dimensions of these structures range from those of ordinary supernova remnants (< 100 pc) to more than 1 kpc, and kinetic energies of expansion are estimated to reach 10^{54} ergs. More recently, galactic-scale *super*bubbles have been found in M82 (Bland & Tully 1988), NGC 253 (McCarthy, Heckman, & van Breugel 1987), and possibly in a few other IR-luminous galaxies (Heckman, Armus, & Miley 1990, hereafter HAM; Veilleux et al. 1994b).

Our understanding of the interaction between the outflowing material and the galaxy ISM has benefited greatly from computational studies (e.g., Castor, McCray, & Weaver 1975, hereafter CMW; Weaver et al. 1977; Chevalier & Clegg 1985; Schiano 1985; Tenorio-Tagle, Bodenheimer, & Rózyczka 1987; Ostriker & McKee 1988; Tomisaka & Ikeuchi 1988, hereafter TI; Mac Low & McCray 1988, hereafter MM; Mac Low, McCray, & Norman 1989, hereafter MMN; Norman & Ikeuchi 1989; Koo & McKee 1990, 1992a, b; Smith, Kennel, & Coroniti 1993). From this work, the general evolution of a windblown bubble can be summarized as follows. In the initial "free expansion" (adiabatic) phase, the kinetic energy that is injected by supernovae and stellar winds ("fast winds" in the nomenclature of Koo & McKee 1992a) is rapidly thermalized via shocks, with little energy lost to radiation because of the very high postshock temperatures and low densities. As the bubble boundary is pushed outward, a dense shell accumulates ISM gas and gradually slows to much less than the wind velocity. This leads to a "four-zoned" bubble with shocked wind between the freely flowing wind and the shell of shocked ISM (CMW; Weaver et al. 1977). Once the shell has expanded and decelerated sufficiently so that its cooling time is shorter than the expansion time, it cools radiatively (radiative or "snowplow" phase). If at any point after

[1] Institute for Astronomy, University of Hawaii, 2680 Woodlawn Drive, Honolulu, HI 96822.
[2] Postal address: Kitt Peak National Observatory, NOAO, P.O. Box 26732, Tucson, AZ 85726-6732; E-mail: veilleux@noao,edu.
[3] Hubble Fellow.
[4] Department of Physics and Astronomy, University of North Carolina, CB 3255, Chapel Hill, NC 27599-3255.
[5] Department of Space Physics and Astronomy, Rice University, Houston, TX 77251-1892.
[6] Department of Astronomy, University of California, Berkeley, CA 94720.
[7] Presidential Young Investigator.
[8] Palomar Observatory, 105-24 Caltech, Pasadena, CA 91125.

shell formation the windblown bubble reaches dimensions comparable to the scale height of the galaxy disk, the shell accelerates outward, begins to fragment through Rayleigh-Taylor instabilities, and injects these fragments and the freely flowing and shocked wind into the galaxy halo. The duration of each phase depends on the nature of the energy source and the structure of the ISM.

Although a good match generally exists between the observed morphology of windblown features and the predictions of these numerical simulations, several discrepancies persist. Notably, the predicted velocities of the shell fragments are often considerably smaller than those observed (MMN; Tenorio-Tagle et al. 1987; Tenorio-Tagle & Bodenheimer 1988). In addition, most of the simulations have considered only a single-phase ISM. Such deficiencies may be resolved with more realistic simulations. For instance, only recently has it been possible to quantify the effects of galactic magnetic fields on the dynamics of windblown bubbles (e.g., Tomisaka 1990; Ferrière, Mac Low, & Zweibel 1991; Slavin & Cox 1992; Mineshige, Shibata, & Shapiro 1993).

To guide the modelers, it is clearly crucial to study in detail the few examples of galaxy-scale, windblown superbubbles. The different bubble zones cool most efficiently at widely different temperatures, requiring flux measurements across the spectrum. The contrast of zones against the surrounding galaxy is low, and spectrophotometry is necessary to isolate the bubble gas from the background ISM by its unusual kinematics and gaseous excitation.

The superbubble in the edge-on SB(s)c galaxy NGC 3079 is very well suited for this type of analysis (cf. Table 1). There is strong evidence for intense star formation in the circumnuclear region of this nearby galaxy. Its very high IR luminosity is similar to that of M82 (Soifer et al. 1987). It exhibits extended 10 μm emission (Lawrence et al. 1985) and harbors the most luminous known extragalactic H_2O maser (Henkel et al. 1984; Haschick & Baan 1985; Haschick et al. 1990). CO maps reveal a bright molecular disk centered on the nucleus and extending to $\sim 15''$ radius (Young, Claussen, & Scoville 1988; Irwin & Sofue 1992; Sofue & Irwin 1992; Tilanus & Veilleux 1994). Optically, the galactic disk of NGC 3079 is well defined and rich in H II regions. The line emission of the nucleus is LINER-like (Heckman 1980), and the Hα spectral profile has faint, broad wings (Carozzi 1977; Stauffer 1982; Keel 1983) that resemble those found in low-luminosity Seyfert 1 nuclei like M81 (Filippenko & Sargent 1988). On closer inspection, however, the line emission responsible for the broad wings in the Hα profile arises from a complex of extranuclear high-velocity clouds (HAM; Filippenko & Sargent 1992, hereafter FS) that coincide with a looplike structure first discovered in Hα + [N II] images (Ford et al. 1986).

TABLE 1

PROPERTIES OF NGC 3079

Parameter	Value	References
Morphological type	SB(s)c	1
Heliocentric velocity (km s^{-1})	1128	2
Distance (Mpc)	17.3	3
Spatial scale (pc arcsec^{-1})	84	3
B_T (mag)	11.54	1
J (mag)	11.85	4
H (mag)	10.52	4
K (mag)	9.77	4
L (mag)	9.16	4
M (mag)	9.41	4
N (mag)	5.46	4
Q (mag)	3.55	4
D_{25}	7'.9	1
Inclination	84°	2
P.A. major axis	166°	2
$L_B (L_\odot)$	1×10^{10}	1
$L_{FIR} (L_\odot)$	3.5×10^{10}	5
$M_{H_2} (M_\odot)$	1×10^{10}	6
$M_{HI} (M_\odot)$	8×10^9	2
L(0.5–4.0 keV) (ergs s^{-1})	2×10^{40}	7

REFERENCES.—(1) de Vaucouleurs et al. 1991; (2) Irwin & Seaquist 1991; (3) Tully et al. 1992; (4) Lawrence et al. 1985; (5) Soifer et al. 1987; (6) Irwin & Sofue 1992; (7) Fabbiano et al. 1992.

The nucleus of NGC 3079 is the optical counterpart to 4C 55.19, a radio source first described by de Bruyn (1977) and Seaquist, Davis, & Bignell (1978) as a cross at the nucleus with linear, partially resolved features extending along the minor axis of the galaxy. More recent maps have resolved a spectacular "figure eight" pattern centered on the nucleus, and extending more than 2 kpc on either side of the galaxy disk along the polar axis (Hummel, van Gorkom, & Kotanyi 1983; Duric et al. 1983; Hummel, van der Hulst, & Dickey 1984; Duric & Seaquist 1988, hereafter DS). Further evidence of activity comes from VLBI maps of the nuclear core by Irwin & Seaquist (1988) which show three aligned sources within the central parsec. Irwin and Seaquist argue that the positions, sizes, and fluxes of each component suggest a jet outflow from a central compact object rather than radio supernovae from a spatially extended starburst. Finally, the X-ray emission extends several arcminutes from the nucleus roughly perpendicular to the galaxy disk (Fabbiano, Feigelson, & Zamorani 1982; Fabbiano, Kim, & Trinchieri 1992; Reichert, Mushotzky, & Filippenko 1993).

The relative importance of the active galactic nucleus (AGN) and the nuclear starburst in powering this outflow is unclear. One reason for this uncertainty is the kinematic complexity of the high-velocity gas and, therefore, the difficulty in determining accurately the kinetic energies of the outflow. The optical long-slit studies of HAM and FS have had only partial success in defining the geometry and kinematics of the outflowing gas because of their sparse spatial coverage. In this paper, we present the results of a study that uses the powerful technique of Fabry-Perot imaging spectroscopy to provide complete two-dimensional coverage of the line-emitting gas. A preliminary analysis was presented by Veilleux et al. (1990). We describe the methods used for the observation and the reduction of the data in §§ 2 and 3. The results are presented and analyzed in § 4. In § 5, we discuss the implications of these results, focusing on the dynamics and the source of energy that drives the outflow. Our conclusions are summarized in § 6.

2. OBSERVATIONS

2.1. *Imaging Spectrophotometry*

The Hawaii Imaging Fabry-Perot Interferometer (HIFI: Bland & Tully 1989) was used on 1990 March 14–17 at the Cassegrain focus of the Canada-France-Hawaii 3.6 meter telescope to produce complete grids of Hα and [N II] $\lambda\lambda$6548, 6583 emission-line profiles across the full optical extent of NGC 3079. These spectra were detected with a low-noise (7.9e^- rms readout) 540 × 540 pixel Ford Photometrics CCD in photometric conditions and with average seeing of $\sim 1''$. The f/2 beam of this instrumental setup resulted in a pixel scale of 0".57.

A finesse 60 etalon with free spectral range 92 Å at Hα was used in its 71st and 72d orders to yield a velocity resolution of 70 km s^{-1} (Nyquist sampling). Order separating filters with a flat-topped transmission profile centered at 6555, 6590, and 6614 Å and 55 Å FWHM bandpass passed only one etalon order, so true emission-line profiles could be synthesized. 137 exposures (velocity slices) representing a total integration of nearly 20 hours were made to cover ± 1500 km s^{-1} on each side of the Hα + [N II] complex, to allow study of the full range of radial velocities in the circumnuclear region. The images were taken at random wavelengths within this range to minimize seeing variations and other time-dependent effects. Instrumental stability was monitored throughout the night by periodically imaging a diffused neon lamp at a nominally constant etalon spacing. A constant ring center showed that no shifts occurred in the etalon optical axis, while a constant ring radius showed no significant variations in the pressure and humidity that would alter the optical gap and capacitance micrometry, respectively. In some spectra, bright sky lines could also be used during the data reduction to verify this result (cf. § 3.1). At the beginning or end of the night, series of exposures were made of the neon lamp and of a current-stabilized flat continuum lamp for wavelength calibration and flat-fielding purposes, respectively. The flat-field exposures were obtained at the same etalon spacing as the data. To provide an absolute flux calibration, the photometric standard stars Feige 34 and θ Vir were observed with the same setup.

2.2. *Long-Slit Spectrophotometry*

Long-slit spectra were obtained in 1985 and 1988 with the Double Spectrograph (Oke & Gunn 1982) at the Cassegrain focus of the Palomar 5-meter telescope. These spectra complement the Fabry-Perot data by extending the wavelength coverage to provide additional line diagnostics. Gratings with 1200 and 600 grooves mm^{-1} were used in the first order to provide spectral resolutions (FWHM) of ~2.5 Å and ~4 Å, over the wavelength ranges λλ6220–6850 and λλ4220–5100, respectively. TI 800 × 800 CCDs were used for both datasets. The spatial scales are 0.″58 $pixel^{-1}$ for the red spectra, 0.″4 $pixel^{-1}$ for the blue spectra obtained in 1985, and 0.″8 $pixel^{-1}$ for the blue spectra obtained in 1988. The slit was always 2″ wide. Spectra of the illuminated dome and of a neon/iron/argon lamp were obtained for flat-fielding and wavelength calibration purposes, respectively. The bright secondary standard stars of Oke & Gunn (1983) were observed as absolute flux calibrators. Most of these spectra were obtained under 1″–2″ seeing, and many nights were judged to be photometric. The journal of observations and slit orientations/positions is given in Table 2. A kinematic analysis of the red 1985 spectra was published in FS.

3. DATA REDUCTION

3.1. *Imaging Spectrophotometry*

The Fabry-Perot data for each of the four nights were reduced independently on a SUN Sparc 330 workstation, using the procedures that are described by Bland & Tully (1989), Cecil, Bland, & Tully (1990), and Veilleux, Tully, & Bland-Hawthorn (1993). In brief: a constant bias value was subtracted from each image, and the images were subsequently stacked into a data cube in increasing order of wavelength. High and low spatial frequencies in the data from pixel-to-pixel sensitivity variations, filter transmission curvature, and detector sensitivity were removed by using a similarly constructed white-light cube. The stability of the instrument was checked by examining the ring centers and radii of a few sky lines throughout each cube to confirm that the centers were stable and that the radii were monotonically increasing. The frames were then spline-shifted to align the centroids of three bright stars in the field (drifts were generally less than 1 pixel). The stellar-continuum background was contaminated by two additive sources: a spatially uniform sky continuum and a non-uniform but smoothly varying component due to moonlight leaks in the instrument adapter. The mean level of the first source was established from a region free of galaxy light, then subtracted from each frame. The residual sky continuum was removed by fitting and subtracting an inclined plane. Cosmic rays were removed by median filtering each spectrum above an empirically determined threshold and with the added condition that the candidate anomalies be spikes in only one veloc-

TABLE 2

JOURNAL OF OBSERVATIONS

Spectrometer	UT Date	Wavelength coverage (Å)	P.A.	Slit Location
Fabry-Perot	1990 Mar 14	redshifted [N II] λ6583	...	...
Fabry-Perot	1990 Mar 15	redshifted [N II] λ6548	...	...
Fabry-Perot	1990 Mar 16	redshifted Hα	...	...
Fabry-Perot	1990 Mar 17	redshifted [N II] λ6548	...	...
Long slit	1985 Feb 24	4220–5100, 6220–6850	−10°	0.″7 E, major axis
Long slit	1985 Feb 25	4220–5100, 6220–6850	+80	Nucleus, minor axis
Long slit	1985 Feb 26	4220–5100, 6220–6850	+45	Nucleus
Long slit	1985 Feb 27	4220–5100, 6220–6850	+135	Nucleus
Long slit	1985 Feb 27	4220–5100, 6220–6850	−10	Nucleus, major axis
Long slit	1985 Feb 28	4220–5100, 6220–6850	−10	2″E, major axis
Long slit	1985 Feb 28	4220–5100, 6220–6850	−10	4″E, major axis
Long slit	1988 Apr 9	4220–5100, 6220–6850	−10	Nucleus
Long slit	1988 Apr 9	4220–5100, 6220–6850	−10	2″NNE, major
Long slit	1988 Apr 9	4220–5100, 6220–6850	−10	4″NNE, major
Long slit	1988 Apr 9	4220–5100, 6220–6850	−10	6″NNE, major
Long slit	1988 Apr 9	4220–5100, 6220–6850	−10	8″NNE, major
Long slit	1988 Apr 9	4220–5100, 6220–6850	−10	11″NNE, major
Long slit	1988 Apr 9	4220–5100, 6220–6850	−10	13″NNE, major
Long slit	1988 Apr 9	4220–5100, 6220–6850	−10	2″SSW, major
Long slit	1988 Apr 9	4220–5100, 6220–6850	−10	4″SSW, major

ity channel. The intensity of the individual frames was also scaled appropriately to correct for (mean) extinction at the mid-exposure air mass of the frame.

The final, most delicate step was to remove the sky line-emission. First, each spectrum was shifted in velocity to correct for the curvature of the isovelocity surfaces ("nested paraboloids"; Bland & Tully 1989). The amplitudes of these shifts were found from the shape of the neon emission line of the calibration cube. The lack of curvature of the night-sky line (or surface) over the full field of view in the *corrected* data cube confirmed the high level of accuracy of this "phase calibration" procedure. In the first iteration, the intensity and profile of the sky line emission were assumed to be constant spatially (temporally). The night-sky line spectrum was found from a region free of galaxy light and subtracted from the data. Next, all spectra were reset to their original position to reveal sky line residuals (rings) caused by temporal variations of the night sky lines, flatfield errors, etc. The final step in the sky-line removal was to fit and subtract any rings with off-center Gaussian intensity profiles to these residuals. This method of removing sky lines worked very well for the Hα and [N II] λ6583 spectral regions. However, residual flux from a very strong sky line near [N II] λ6548 affected the faintest parts of this line.

Next, slight positional shifts (again less than 1 pixel) between the cubes from each of the nights were removed to align the data, and each cube was scaled by a small multiplicative factor to correct for slight transparency variations between nights. The cube of night 3 (covering most of Hα) served as the reference because it was obtained in the most stable conditions. The scaling factors were found by comparing regions of spectral overlap at the nucleus, in a few bright H II regions, and in one or two bright field stars. Correction factors were −5%, +11%, and +37% for nights 1, 2, and 4, respectively. The uncertainty of these numbers was estimated to be ±2%–3%, and is dominated by errors associated with the flatfield curvature at the edge of the filter transmission profiles. Once combined into one cube, the data were phase calibrated using the curvature previously found from the sky-line removal.

The zero point of the velocity scale was derived from the positions of a Neon calibration line and the OH sky lines at 6544.02 and 6553.61 Å (Osterbrock & Martel 1992). Finally, the spectra were placed on an absolute flux scale by comparing the raw counts from photometric standard stars on all four nights with the absolute fluxes tabulated in Stone (1977) for Feige 34 and Goodrich & Veilleux (1988) for θ Vir. Our fluxing procedure is detailed in Bland-Hawthorn, Shopbell, & Veilleux (1994); an "effective bandpass" of 2.4 Å was derived from the Neon line profiles in the calibration cubes.

3.2. *Long-Slit Spectrophotometry*

Standard VISTA and IRAF procedures were used to produce wavelength calibrated, sky-subtracted, fluxed long-slit spectra. When the slit was oriented along the major axis of the galaxy, line emission from the galaxy extends over its full length, so the sky spectra were found from the uncontaminated portions of the spectra of smaller galaxies that were obtained shortly before or after the observations of NGC 3079. Appropriate scale factors for the sky spectra were calculated by examining the residual background and sky lines. (The [O I] λλ6300, 6364 lines were not considered for this procedure because their fluxes varied in time much more than the background continuum.) We attempted to correct the emission lines for underlying stellar absorption by subtracting a scaled nuclear spectrum of the S0 galaxy NGC 3115, obtained with the same setup as NGC 3079. The absorption-line correction was particularly important when determining the intensity of the Hβ emission line.

4. EMPIRICAL RESULTS

The Fabry-Perot and long-slit spectra described in the previous two sections provide gaseous kinematics and line fluxes across the optical disk; ~50,000 emission-line spectra were produced with the Fabry-Perot. Automated analysis showed that the line-emitting gas in the disk is relatively quiescent, with emission-line profiles generally well approximated by a Gaussian. In contrast, the nuclear gas presents complex motions and excitation properties that differ markedly from gas elsewhere. This paper focuses on the processes active in the immediate circumnuclear region. The properties of the line-emitting gas located outside ~40″ radius, including a discussion of the influence of the activity and normal star formation on the disk, will be described elsewhere (Veilleux et al. 1994a, hereafter Paper II).

4.1. *Morphology of the Nuclear Superbubble*

Figure 1 (Plate 1) maps the distribution of the nuclear Hα + [N II] λλ6548, 6583 line emission derived from the Fabry-Perot data cube after removal of the underlying stellar continuum. Note that Galactic reddening is negligible in the direction of this galaxy (Burstein & Heiles 1978, 1984). The faintest features in Figures 1*a* and 1*b* have a surface brightness of about 10 and 1×10^{-16} ergs sec^{-1} cm^{-2} arcsecond^{-2}, respectively. The 20 cm VLA map of DS has been contoured on our emission-line image. A comment on the method used to align the radio and optical data is appropriate because of the report (Lawrence et al. 1985) of a possible shift between the optical and radio/10 μm continuum peaks. For the present data, the position of the 20 cm continuum peak was taken from Irwin & Seaquist (1991) and the position of the optical *emission-line* peak was derived using two bright stars in our field of view whose positions were listed in the *Hubble Space Telescope* Guide Star Catalog (1989). We find that these two positions agree well in declination and coincide within 3″ ± 2″ in right ascension (the emission-line peak may lie east of the radio peak).

Ford et al. (1986) first noted a nearly circular shell of line-emitting gas of diameter 13″ (1.1 kpc at the distance of 17.3 Mpc, cf. Table 1) on the east side of the nucleus. The fainter limiting flux of our data shows that the shell is complete at low intensity levels. Most of the radio emission lies outside the optical line-emitting ring, suggesting that the relativistic, radio-emitting particles have broken through. This will be discussed in greater detail in § 5.4, where we will address the dynamical state of the bubble. The galaxy disk obscures any obvious emission-line counterparts to the *western* radio bubble in Figure 1. However, faint kinematic features associated with the nuclear outflow were detected on this side (cf. § 4.7). Anomalous kinematic features in the inner disk were also discovered, and will be described in § 4.8.

4.2. *Decomposition of Emission-Line Profiles Across the Bubble*

To maximize signal-to-noise ratios of spectra across the bubble, we binned our profiles in strips 2″.3 wide along the galaxy minor (and bubble symmetry) axis at +80° P.A. (Fig. 2 [Pl. 2]). A survey of profiles across the bubble showed that

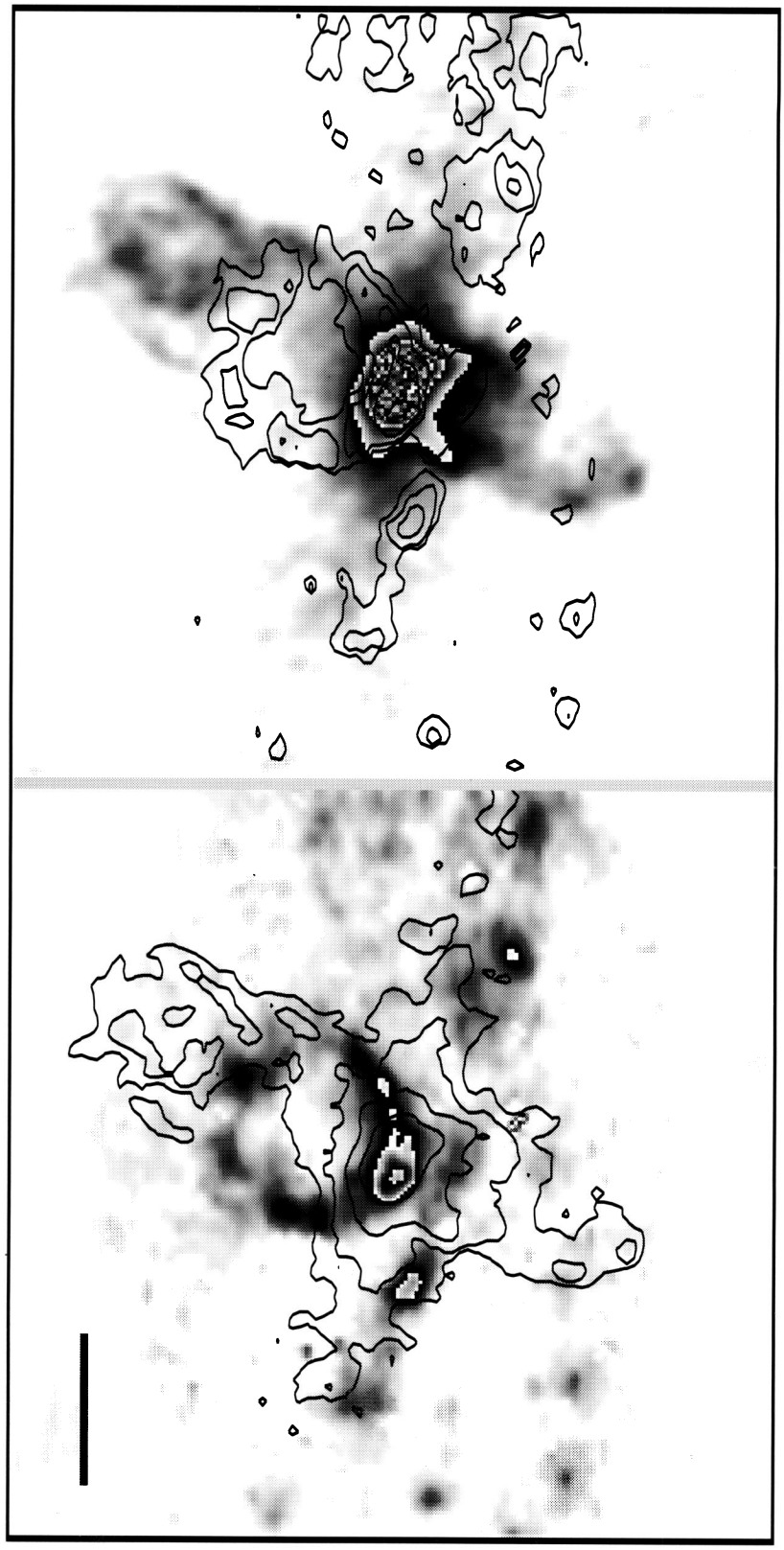

FIG. 1.—Continuum-subtracted distribution of Hα + [N II] λλ6548, 6583 line emission and the 20 cm continuum distribution in the circumnuclear region of NGC 3079. The λ20 cm VLA map of Duric & Seaquist (1988) is plotted as a gray-scale in the top image and as contours in the bottom; vice versa for the line map. North is at the top and east to the left. The spatial scale, indicated by a horizontal bar at the bottom of the image, corresponds to 12″, or 1 kpc for the adopted distance of NGC 3079 of 17.3 Mpc. The logarithmic surface brightness ranges from 3×10^{-15} ergs s^{-1} cm^{-2} $arcsec^{-2}$ in the nucleus down to about 1×10^{-16} ergs s^{-1} cm^{-2} $arcsec^{-2}$.

PLATE 2

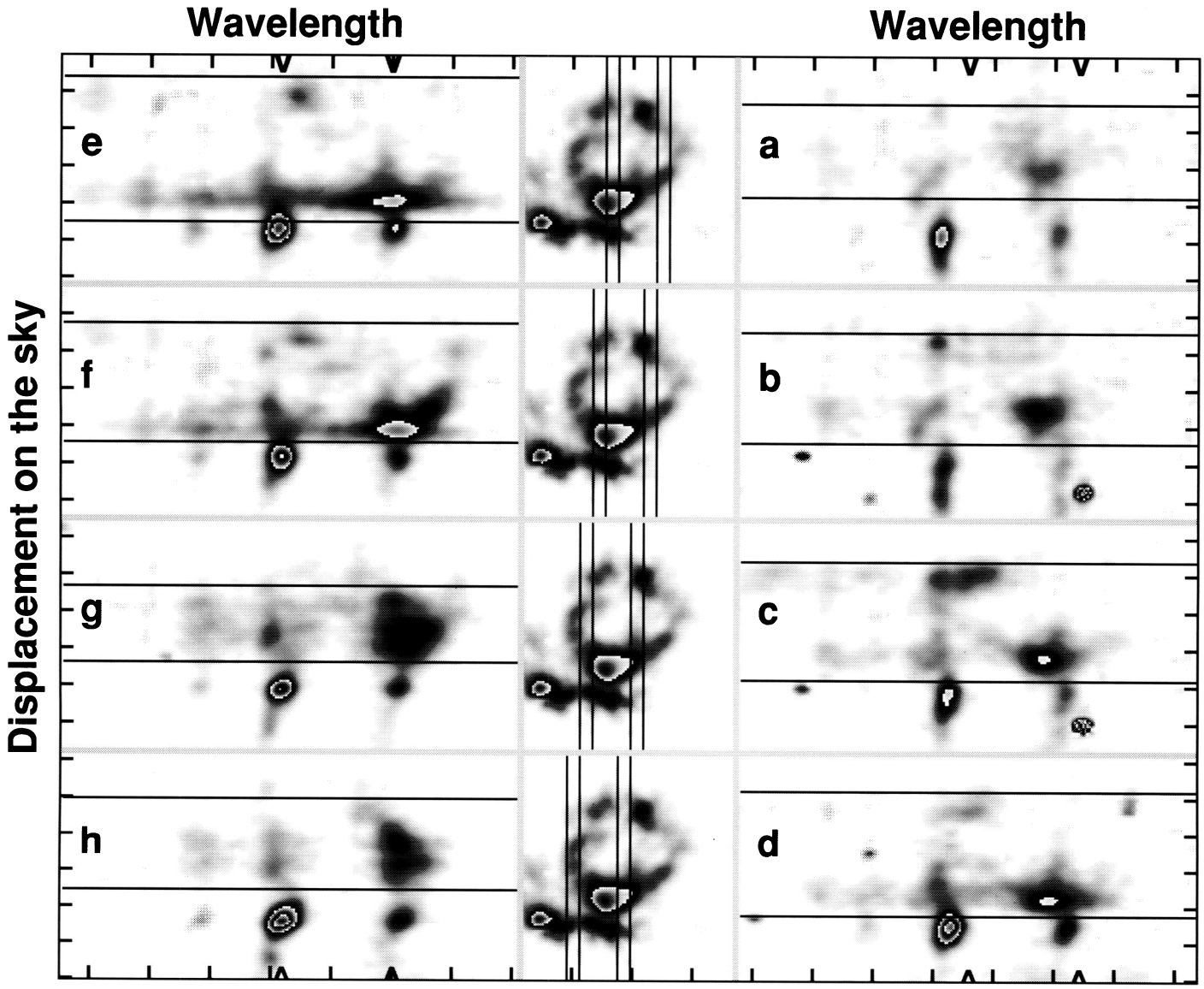

FIG. 2.—"Long-slit" spectra extracted from the circumnuclear region of the Fabry-Perot cube, rotated counterclockwise so that P.A. $-10°$ is at the top and, in the small images, the major axis of the galaxy runs horizontally. The width of each effective slit is 2.″3, and their positions on the bubble are shown in the center. The "long-slit" spectra extracted from the data cube using each pair of effective slits are shown on the left and right, with two horizontal lines showing the spatial range over which the profiles were decomposed with multiple Gaussians; elsewhere, single Gaussians were satisfactory. The thick marks on the vertical axis are 5″ apart, while those on the horizontal axis are 500 km s^{-1} apart. Arrowheads at the top and bottom mark the systemic velocity of Hα and [N II] λ6583. The tilted narrow lines in the spectra arise from residual moonlight in several frames.

most are composed of three distinct velocity systems: blue- and red-wing "bubble" components appear to have near-constant FWHM $\approx$ 350 km s^{-1}, while the "disk" component has FWHM $\approx$ 130 km s^{-1} (after accounting for our instrumental FWHM of 70 km s^{-1}.)

The different components can be isolated, and their spatial distribution mapped, by fitting Gaussian functions. We fit three components to each line in the [N II] $\lambda\lambda$6548, 6583 + Hα complex, fixing the [N II] doublet ratio to its quantum value, and using the same line widths for the blue and red components. Stable fits are found across most of the bubble, and Figure 3 (Plate 3) shows that they satisfactorily reproduce the complex variations. The distributions of line fluxes and velocity centroids are shown in Figures 4 (Plate 4) and 5. The [N II], Hα profiles from the red long-slit spectra have similar signal-to-noise ratios and velocity resolutions, and exhibit similar structure, to those derived from the Fabry-Perot data cube. These data were used to cross-check the profile decomposition derived from the Fabry-Perot data, and the fits seemed reliable and plausible.

Line fluxes peak along the bubble boundaries. Although a few regions with ratios [N II] λ6583/Hα < 1 are found along the northern boundary, Figure 4 shows that the ratios are greater than 2.5 at most points in the bubble. Values this large imply gaseous excitation by shocks or a hard-spectrum photoionizing source (see § 4.6 and § 5.6). We find velocity centroids that are blueshifted from galaxy systemic by up to $\sim$1100 km s^{-1}. We are unable to confirm the extreme velocity blueshifts of 1600 km s^{-1} that HAM reported at one location in the NE quadrant of the bubble. This may reflect the problem, mentioned in § 3.1, with our subtraction of the sky line-emission from the [N II] λ6548 profiles. In regions where the three components are strongly blended, we estimate uncertainties in velocity centroids of $\sim$1 velocity sample = 34 km s^{-1}. Line widths are also difficult to define in these regions, but elsewhere we find no significant width variations across the bubble.

Our velocity decomposition quantifies the asymmetric "bubble" pattern that was first described by FS, based on their long-slit spectra. Our datacube now shows that blueshifted velocities generally exceed those on the red wing, and that both often coexist. This asymmetry in the velocities is larger in the northern half of the bubble. Throughout most of the bubble, the velocity and surface brightness of the wing components are inversely correlated as in planetary nebulae. Velocity splitting is largest along the mid-axis of the bubble.

These patterns support FS's contention that we are looking through an optically thin bubble, to blue and red components that arise from the front aand back volumes. However, our data show velocity patterns that are not seen in planetary nebulae, where gas expands radially from the central star. Instead, in NGC 3079 velocities increase monotonically with nuclear radius until about three quarters of the diameter of the bubble; the high-velocity gas disappears very rapidly beyond this point. This decrease is less abrupt in the SE quadrant of the bubble (*left-hand panels*, Fig. 5). As FS have noted, this flow is consistent with a radially increasing rate of expansion from the nucleus.

4.3. *Kinematic Model of the Superbubble*

To deproject the observed velocities to intrinsic outflow velocities, we need to constrain the phase-space distribution of

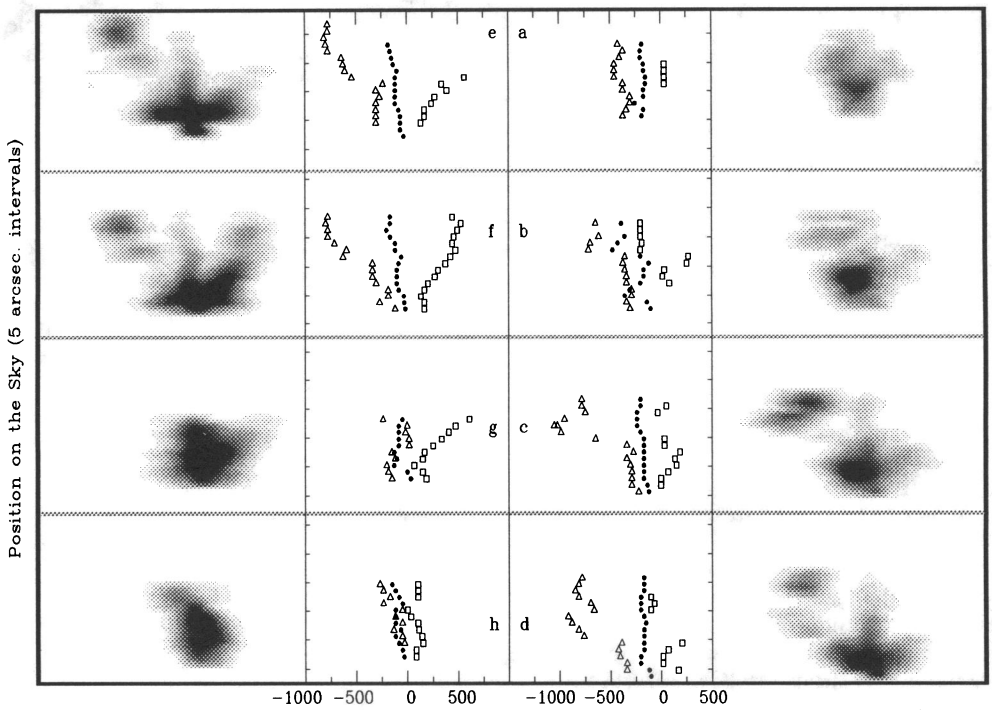

FIG. 5.—Velocity centroids of the emission-line components in the bubble, together with the synthesized model profile as a gray scale. Each panel corresponds to a different "slit" position across the bubble. The label on the center panels shows the correspondence between this figure and Figs. 2–3. In each panel, the vertical axis indicates the positions along the "slit," while the horizontal axis indicates the radial velocities of the components (relative to the systemic velocity of the galaxy). Three components are observed at most points in the bubble: blueshifted (*open triangles*) and redshifted (*open squares*) bubble components, and a systemic disk component (*small filled circles*).

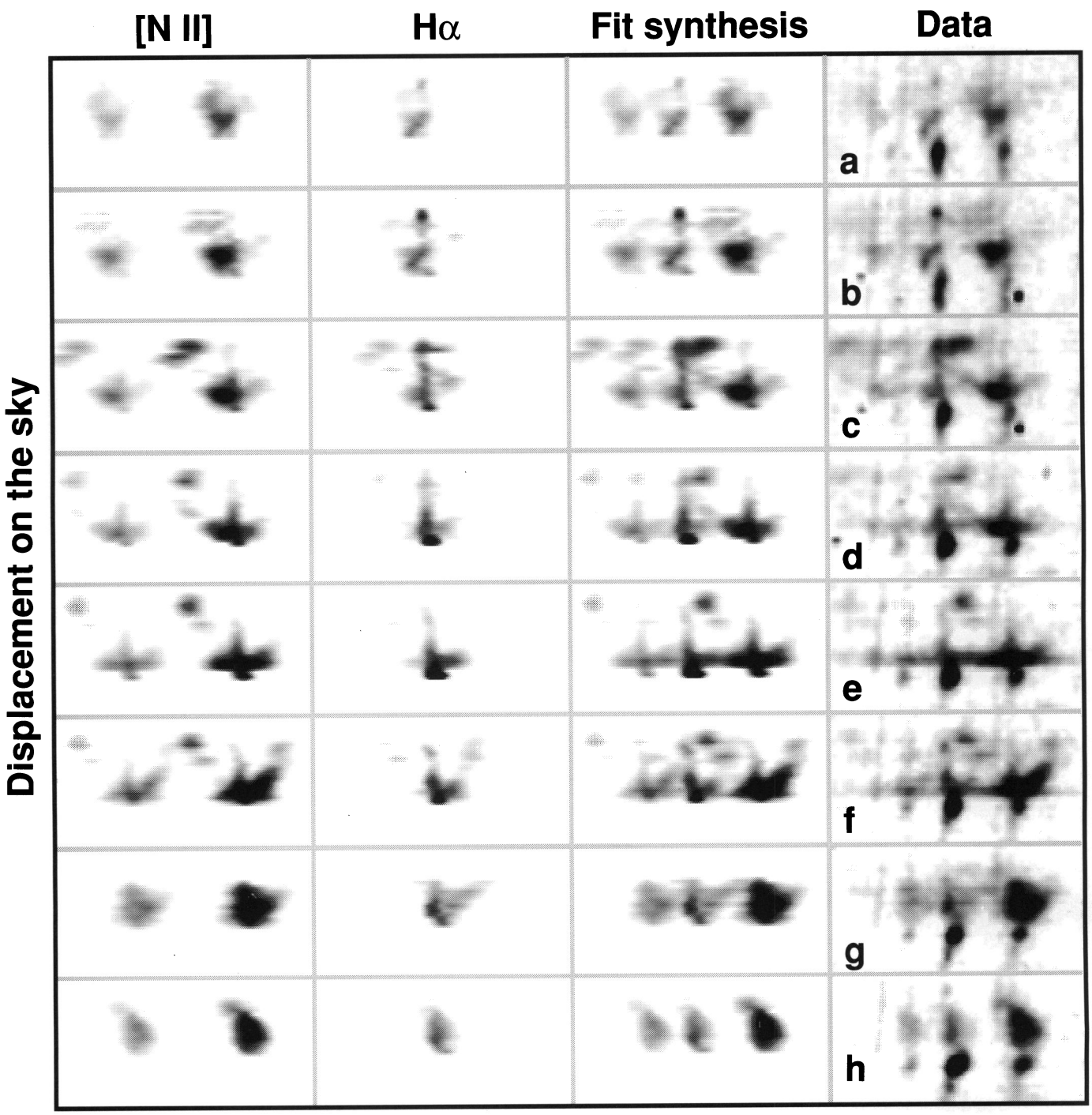

FIG. 3.—Comparison of the fitted emission-line profiles with the reduced spectra after subtraction of the galaxy stellar continuum. The right-hand column shows the data, the third column shows the [N II] λλ6548, 6583 + Hα profiles that are synthesized from our three-component Gaussian fits (see text). In general, profiles beyond the bubble boundaries were adequately fit with single components and are not shown. The first and second columns show the [N II] and Hα components from the fits.

PLATE 4

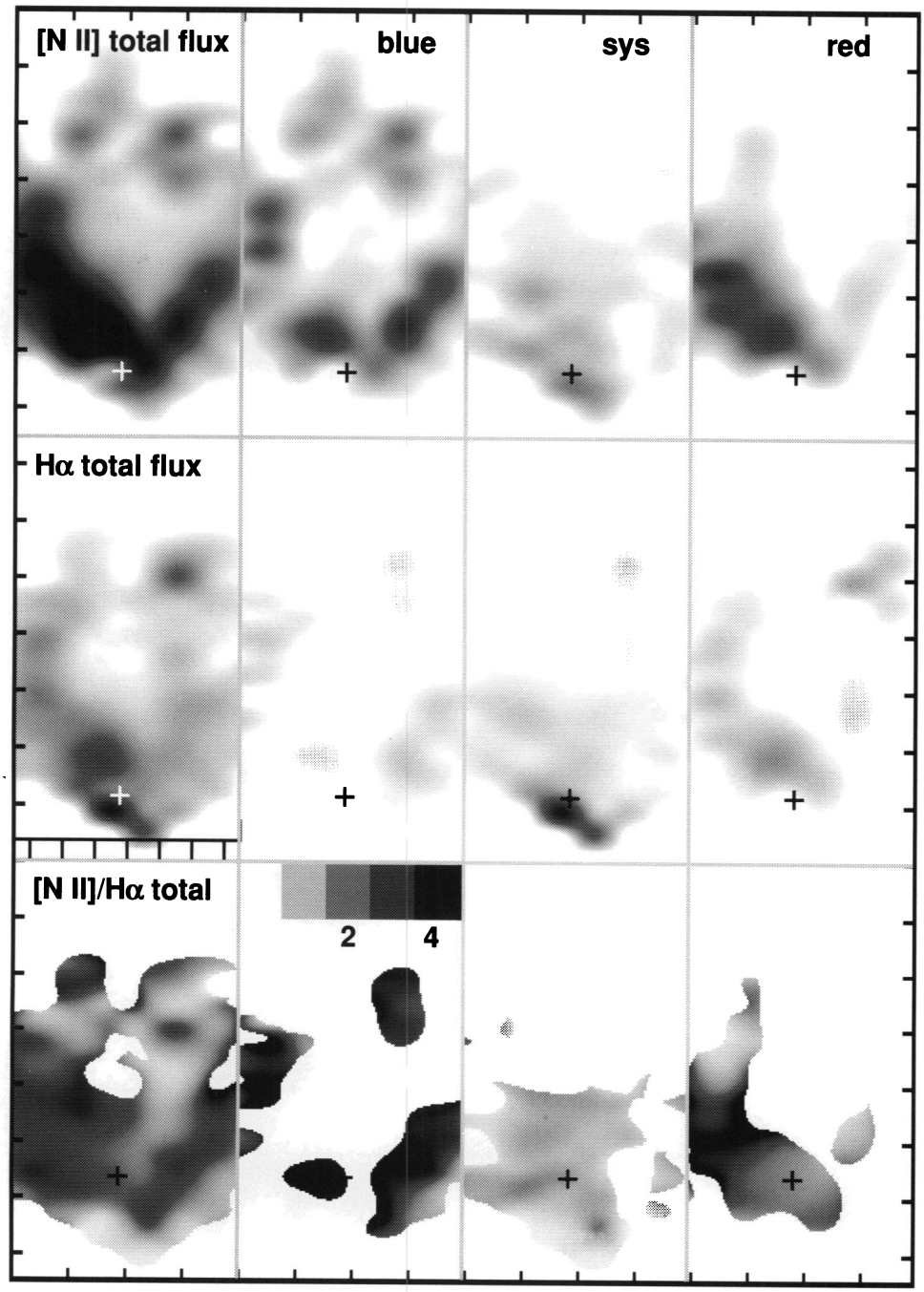

FIG. 4.—Flux distributions across the bubble, derived from multi-Gaussian fits to the emission-line profiles. Ticks at 200 pc intervals, with P.A. – 10° at right. The distributions of [N II] λλ6548 + 6583 and Hα are shown for the blue, systemic, and red components, and their sum. The ratio [N II]/Hα is also shown. The cross indicates the position of the peak intensity of the optical continuum.

the gas within the bubble. The well-defined patterns summarized above show that the gas flow at the boundary has a large-scale organization, so it is reasonable to assume that the bubble is a system of oblique shocks that are driven from a compact nucleus. If the cooling length of the postshock gas is small, we can assume that only the bubble boundary emits optical lines. This restriction still admits a daunting range of possible gaseous flows. The intrinsic velocities that are ultimately projected onto the observed line of sight will be the vector field that results from the interaction of the original wind outflow with the complex of expanding oblique shocks that form the bubble boundary. This interaction can lead to large refractions of the postshock flow away from the local normal at the shock surface, depending on the relative speeds of the outflow and shock propagation and the dynamical state of the shock itself (i.e., whether it strongly radiates or is nearly adiabatic). Furthermore, the observed velocity patterns are *not* rotationally symmetric in azimuth about the bubble mid-axis. Figure 5 shows that the gas component with large redshifted velocities is detected over a broader region than the component with large blueshifted velocities. The only way to reproduce these patterns is to structure the distribution of the high-velocity gas so that it has different angular extent on the bubble front and back sides, with a more extensive back side (redshifted) region. The added ambiguity of the need to specify an azimuthal distribution of high-velocity gas across the bubble surface really limits what we can say about the radial dependence of the outflow velocity.

Unable to seek full dynamical consistency, we will simply parametrize the velocity pattern of the bubble to allow crude—but plausible—deprojection of the observed velocities. In the end, we will find that our conclusions are quite robust. In the following discussion, we ignore azimuthal variations and assume that the bubble is delineated by gas that is accelerating radially from the nucleus such that $V \propto R^n$. We estimate the index n by comparing the projected morphology and velocities of the observed and model bubbles. Other fit parameters to be found are the actual shape of the bubble (spherical, ellipsoidal, or ovoidal), the inclination of the bubble axis with respect to the line of sight, and a characteristic outflow velocity (see Fig. 6). The optically emitting gas is assumed to lie along the boundary of the bubble, and to not be present in the interior. Gas velocities at this surface are assumed to be radial from the nucleus.

An ovoidal bubble with the more pointed end near the nucleus was found to best match the observed morphology of the emission-line structure. Good fits to the observed velocity distribution along the bubble mid-axis were found for $n = 2$–3 (Fig. 7). This figure also shows that larger values of n produce too abrupt a decrease in velocity at large radii, while smaller values produce velocity gradients that are too symmetric about the center of the bubble. With this flow field the abrupt decrease in velocities near the top of the bubble arises when the rapidly increasing velocity vector swings into the sky plane, rather than from rapid deceleration. The bubble axis must be tipped toward us by 2°–4° to produce the observed asymmetry in maximum absolute velocities on the blue and red profile wings (Fig. 5). Note that this value of the inclination implies that the outflow is along the minor axis of the galaxy, within the uncertainties of the measurements (Irwin & Seaquist 1991; Paper II). Figure 8 compares the off-axis velocity field predicted by the $n = 2.5$ and $n = 3.0$ models with the data. There is a clear tendency for these models to overestimate the velocity of the redshifted gas. If we adopt an inclination of 2°5 and $n = 2.5$, the maximum observed velocity along the bubble mid-axis of 1100 km s^{-1} implies peak outflow velocities of the optically emitting gas of 3600 km s^{-1} at the top of the bubble. The masses and kinetic energies of our best outflow model are discussed in §§ 5.2 and 5.3 along with estimates of the second-order effects that were not considered.

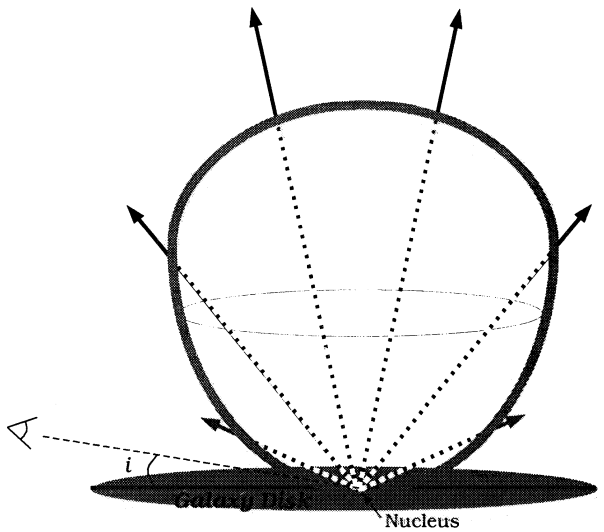

FIG. 6.—Geometry of the kinematic model. The model parameters are the shape of the bubble (spherical, ellipsoidal, or ovoidal), its inclination to our line of sight (which is found to equal the inclination of the galaxy disk, angle i in this figure), some characteristic outflow velocity, and the slope of the velocity gradient n ($V \propto R^n$).

The most likely explanation for the nearly systemic "disk" component is that we are seeing the galactic disk at larger radii through the bubble. The flux distribution of this component does not appear correlated with the bubble emission (Fig. 4). The small [N II]/Hα of this component can be produced by photoionization from hot stars in the disk (cf. Paper II). The lack of any obvious rotation in this component is consistent with the expected velocity field of the disk near the minor axis (Paper II). We will assume in the rest of our discussion that this component is not taking part in the nuclear outflow.

4.4. *Electron Density and Temperature*

The flux ratio of the [S II] λλ6716, 6731 lines was used to constrain the average electron density in the ionized gas of the bubble. The values of this ratio *outside* the bubble are shown in Figure 9. Examples of [S II] decompositions near the nucleus are presented in Figure 10. Although the [S II] lines are each only ~40% the intensity of the [N II] λ6583 line, and strongly blended, it was possible in the brighter regions of the bubble to decompose their profiles into the same three components identified in the nitrogen and hydrogen lines by scaling the [N II] profiles to the sulfur doublet, then varying the amplitudes but fixing the component widths and velocity centroids to those derived for the Fabry-Perot data. We allowed the various components to have different [S II] ratios. We obtained good fits in cases with adequate signal-to-noise ratios, and found that the [S II] λ6716/λ6731 ratio of the systemic component never was below ~1.2, and was in its low-density limit, ≥1.3 (which implies $N_e < 125$ cm^{-3}) even very near the nucleus. The [S II] ratios in the bubble components are only weakly constrained.

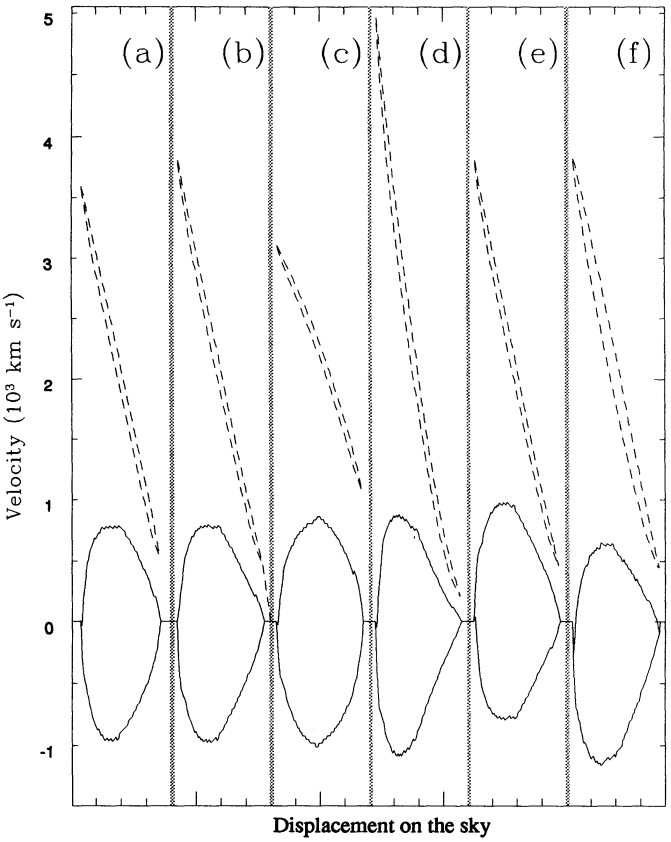

FIG. 7.—Predicted radial (*solid lines*) and unprojected (*dashed lines*) velocities of the models for the front and back sides of the bubble, down its mid-axis. The gas expands leftward from the nucleus, located on the right-hand side of each panel. We show the following parameter sets: (*a*) spherical bubble with $n = 2$, $i = 2°$ and $V(1\ \mathrm{kpc}) = 3600$ km s^{-1}; (*b*) ovoidal bubble with $n = 2$, $i = 2°$, and $V(1\ \mathrm{kpc}) = 3700$ km s^{-1}; (*c*) ovoidal bubble with $n = 1$, $i = 2°$, and $V(1\ \mathrm{kpc}) = 3000$ km s^{-1}; (*d*) ovoidal bubble with $n = 3$, $i = 2°$, and $V(1\ \mathrm{kpc}) = 4700$ km s^{-1}; (*e*) ovoidal bubble with $n = 2$, $i = -2°$, and $V(1\ \mathrm{kpc}) = 3500$ km s^{-1}; (*f*) ovoidal bubble with $n = 2$, $i = 6°$, and $V(1\ \mathrm{kpc}) = 3500$ km s^{-1}. The model that best fits the observed morphology and velocity field of the bubble has an ovoidal geometry with $n = 2$–3, $i = 2°$–4°, and $V(1\ \mathrm{kpc}) = 3600$ km s^{-1}, see Fig. 8.

Nevertheless, *in the bubble we find no indication for* [S II] *densities substantially above the low-density limit.* The discrepancy between this result and the continuous density gradient by HAM (their Fig. 13) is probably due to the very limited spatial coverage of the long-slit data of HAM. Our analysis also allows us to investigate densities close to the nucleus where the lines are blended because it incorporates fit constraints from stronger lines.

Our results invalidate HAM's size estimate of the energy injection zone, an argument they used to favor a starburst origin for the outflow in this galaxy. The compactness of the radio flux and spectral index distributions in this galaxy (DS) suggests a small ($R \lesssim 100$ pc) energy injection zone, but this result does not exclude the possibility that the nuclear region of the starburst powers the outflow (§ 5.3). *Lower* limits on the densities will be derived in § 5.3 from dynamical arguments.

Neither of the two optical line ratios most often used to measure temperatures ([O III] λ4363/λ5007 and [N II] λ5755/λ6583) were accessible in our long-slit spectra. [N II] λ5755 lies outside the wavelength range of our data, while [O III] λ4363 is extremely faint and badly blended with relatively strong residual sky and stellar absorption lines that remain after subtraction of the scaled spectrum of NGC 3115.

4.5. *Extinction*

The extinction of the line-emitting gas was estimated with the Hα/Hβ flux ratio from the long-slit spectra. Hβ emission was often weak and strongly reduced by underlying stellar absorption. Therefore, the Balmer decrement could be measured only when Hβ was strong: in the nucleus $\sim$18, and $\sim$5–7 near the base of the bubble (2″–8″ radius). Uncertainties are typically 25%–50%. The reddening curve described by Mathis (1990) and Cardelli, Clayton, & Mathis (1989) was used to translate these decrements into dust optical depths at Hα. We adopt an intrinsic Hα/Hβ ratio of 2.86 (case B recombination for $T = 10^4$ K and $N_e = 10^2$ cm^{-3}); note that a similar ratio is predicted for shock excitation (e.g., Binette, Dopita, & Tuohy 1985, hereafter BDT; cf. § 4.6). We obtain τ(Hα) $\sim$ 4 in the nucleus and $\sim$1–2 near the base of the bubble. Such a steep gradient in dust optical depth is not surprising because the galactic disk of NGC 3079 is nearly edge-on. It is also consistent with the presence of the compact molecular disk observed by Young, Claussen, & Scoville (1988). Recent high-resolution maps show that this molecular disk is roughly aligned with the galaxy major axis and has a total thickness of $\sim$200 pc (Irwin & Sofue 1992; Sofue & Irwin 1992; Tilanus & Veilleux 1994).

4.6. *Excitation Properties of the Line-Emitting Gas*

In § 4.2 we noted the very large [N II]/Hα ratios across the bubble. Additional line ratios were found from the long-slit spectra and, like [N II]/Hα, were almost constant across the bubble: [O III] λ5007/Hβ = 2.5–5.0, [S II] $\lambda\lambda$6716, 6731/Hα = 0.6–0.9, and [O I] λ6300/Hα = 0.1–0.2 (e.g., Fig. 9). The [S II]/Hα ratio is the most reliable of these three ratios because the [S II] lines are stronger than [O I] λ6300, and Hα is considerably less effected than Hβ by underlying stellar absorption.

These line ratios differ significantly from those found in normal H II regions, so are difficult to explain through photoionization by hot stars of gas having normal solar abundance (e.g., Baldwin, Phillips, & Terlevich 1981, hereafter BPT; McCall, Rybski, & Shields 1985; Veilleux & Osterbrock 1987, hereafter VO87). Other processes produce line ratios similar to those seen in the bubble: (1) shock ionization when the outflowing gas collides with the ambient ISM of the galaxy (Heckman 1980; Shull & McKee 1979; BDT; Innes 1992; Dopita 1994), (2) photoionization by a weak or heavily attenuated AGN continuum (Ferland & Netzer 1983; Filippenko & Halpern 1984; Péquignot 1984; Stasińska 1984; Binette 1985; Filippenko 1985; VO87), (3) photoionization by a population of hot, high metallicity stars in a dense environment (Terlevich & Melnick 1985; Terlevich 1992; Filippenko & Terlevich 1992; Shields 1992), (4) photoionization by EUV/X-ray radiation emitted by cooling filaments in the outflow or by the shocked wind material itself (Schiano 1985; Donahue & Voit 1991; Slavin, Shull, & Begelman 1993; Smith et al. 1993), (5) heating of a photoionized region by cosmic-ray particles that are trapped in magnetic fields (Ferland & Mushotzky 1984; César, Viegas-Aldrovandi, & Gruenwald 1985; Gruenwald & Viegas-Aldrovandi 1987; Viegas-Aldrovandi & Gruenwald 1988). Although additional line diagnostics from higher excitation species are required to discriminate most effectively

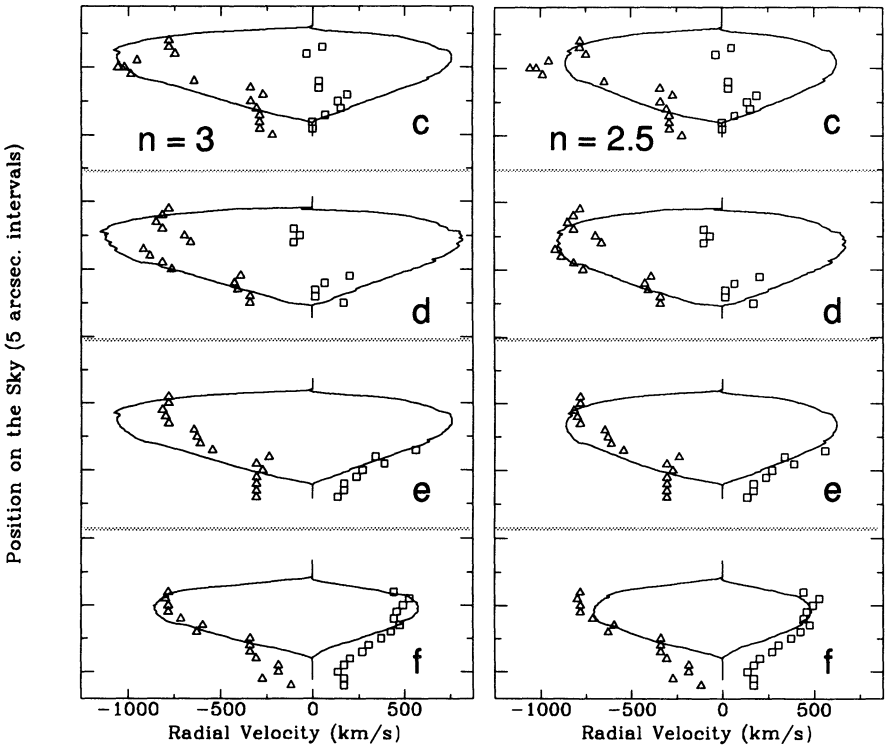

FIG. 8.—Comparison of sample kinematic models with the data as sampled with 4 "long-slits" across the bubble. The label on each panel shows the correspondence between this figure and Figs. 2, 3, and 5. The left-hand plot shows the model for which velocities are increasing as R^n with $n = 3$, while the right-hand plot shows the model with $n = 2.5$. Both models are inclined by $i = 2°.5$ to the line of sight.

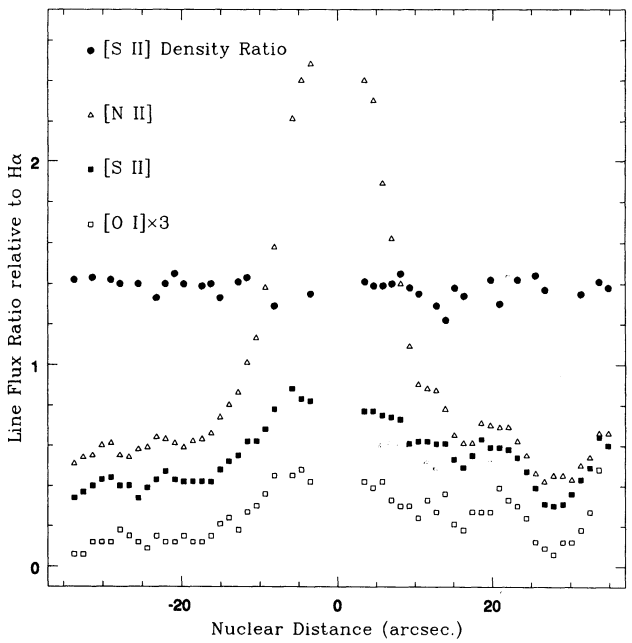

FIG. 9.—Emission-line ratios derived from single component Gaussian fits to the long-slit spectrum 1 that crosses the bubble base and is centered 0".7 E of the nucleus, along P.A. −10°. The [O I] λλ6300, 6364 flux has been tripled for clarity. The [S II] density ratio shows that the ionized gas is in its low-density limit ($n_e < 125$ cm^{-3}) at most points along the slit and across the bubble base. Not shown in this figure are the [S II] density ratios determined in the bubble through constrained multi-Gaussian fits. These are also found to be in the low-density limit (see Fig. 10).

between these alternatives, our data provide constraints, as we now describe.

The violent motions observed across the bubble are highly supersonic, so high-velocity (100 km s^{-1} $\lesssim V_s \lesssim$ 500 km s^{-1}) shocks will contribute to the ionization of the line emitting gas. The upper limit on the shock velocities is set by requiring that the cooling time scale be less than the age of the bubble (cf. § 5.6, eq. [15]). The strong correlation observed between the surface brightness of the individual components and their [N II]/Hα ratio (Fig. 4) is predicted by shock ionization. However, comparing our line ratios with the predictions of BDT, we find that none of the *steady-state* models can reproduce all of the observed line ratios simultaneously. The post-shock material in such strong shocks is expected to undergo a cooling instability (e.g., Field 1965), so the predictions of steady-flow shock models with shock velocities larger than ~100 km s^{-1} are unreliable. Therefore, BDT also investigated the effects of thermal instabilities of the output spectrum using finite age/optically thin models. The effect is to increase the line fluxes to hydrogen of high-excitation species like O^{++} and, to a lesser extent, N^+. The optically thin model investigated by BDT ($V_s = 268$ km s^{-1}) satisfactorily reproduces the [O III]/Hβ and [N II]/Hα ratios for a shock age of order 5×10^{10} yr, but it predicts [O I]/Hα and [S II]/Hα ratios that are larger than the observed values.

Recently, Innes (1992) calculated more self-consistently the spectra emitted from high-speed shocks, accounting for the time dependence of these thermally unstable models and for cushioning by interstellar magnetic fields. Although, again, a very narrow range of shock parameters was investigated, com-

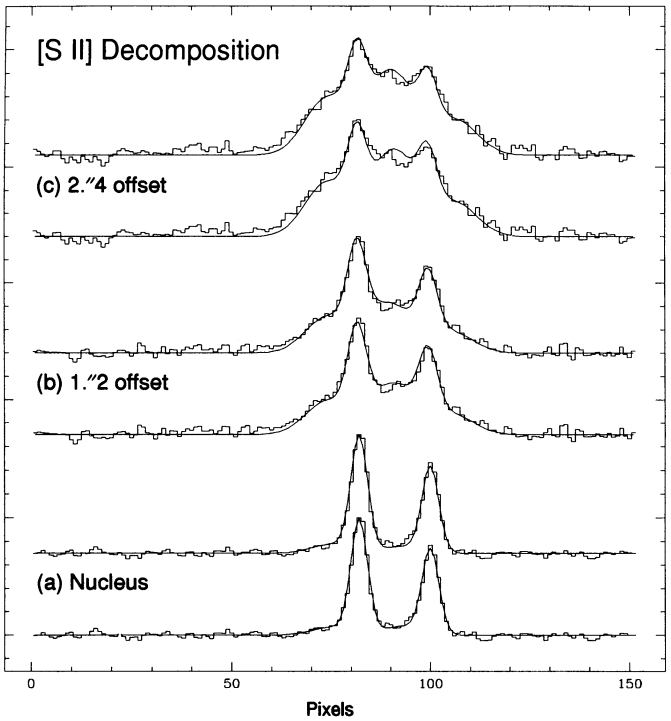

FIG. 10.—Fits to the [S II] doublet at the nucleus and near the base of the superbubble. Each profile is the sum of two spectra along the long-slit, and so spans 1."2 eastward along P.A. $-10°$ and is 2" wide. Then each profile was smoothed to the spectral resolution of the Fabry-Perot data cube. Finally, each line in the [S II] doublet was fit with the same two or three Gaussian components that were isolated in each line of the [N II] $\lambda\lambda$6548, 6583 + Hα complex (Fig. 5). In the fit, only the relative intensities of the blue- and red-wing Gaussian components in the [S II] λ6716 line were allowed to vary; the "systemic" component was fixed at the low-density limit. In addition, the ratio [S II] λ6716/λ6731 was fixed at 0.85 (corresponding to log $n_e \approx 2.9$) for the bottom and 1.3 (corresponding to log $n_e \approx 2.1$, the low-density limit) for the top spectrum in each pair shown in the figure. The fits are better if the bubble gas near the nucleus is at the low-density limit rather than the higher densities found in other superwinds at these radii (Fig. 13 of HAM.)

binations of large [N II]/Hα and moderate [O III]/Hβ are easily reproduced in non-steady models with $V_s \approx 175$ km s^{-1}. However, as in BDT's calculations, these models tend to overproduce [S II]/Hα and [O I]/Hα. Simulations covering a larger range of shock velocities need to be computed for an adequate comparison with our data (cf. Dopita 1994). The possibility that nitrogen is overabundant with respect to the solar value should also be investigated.

The photoionization models have difficulty explaining the extreme line ratios that we observe in NGC 3079 unless the metallicity (and especially the nitrogen abundance) is higher than the solar value. This possibility cannot be excluded and may be a natural consequence of intense nucleosynthesis in the inner galaxy either through star formation (Young et al. 1988) or in the putative accretion disk of the AGN itself (Guessoum & Gould 1989). However, we will show in § 5.2 that a large portion of the bubble gas is probably entrained ISM from the galaxy disk and is thus likely to have near-solar metallicity. The lack of spatial variations of [O III] λ5007/Hβ, an emission-line ratio that is particularly sensitive to the ionization parameter (≡ density of ionizing photo/electron density; e.g., Ferland & Netzer 1983), suggests that photoionization by a hard continuum emitted by a *nuclear* source (AGN or very hot stars) is *not* the dominant ionization process in the bubble unless the density declines as $N_e \propto R^{-2}$. The lack of any steep radial gradients in the surface brightness ($\propto N_e^2$) of the bubble makes this unlikely. On the other hand, the possibility that photoionization by an *extended* source of hard photons is the dominant ionization source cannot be rule out (scenarios 3 and 4).

Most likely, a combination of these processes is contributing to the ionization of the gas in the bubble region. Constraints on the relative importance of shock ionization will be derived in § 5.6.

4.7. *Optical Counterparts to the Western Outflow*

Figure 11 (Plate 5) shows "long-slit" spectra extracted from the Fabry-Perot datacube along the major axis of the galaxy. Each panel corresponds to a different western offset from the nucleus. Gas not in galactic rotation is evident at fainter intensity levels. A large coherent structure with non-rotational velocities (hereafter called the "incomplete western bubble") is at P.A. = 230°–290° and extends over the radial range 10"–14" or 840–1200 pc from the nucleus (Figs. 11*c* and 11*d*). A few isolated emission-line blobs having smaller velocities are also detected closer to the nucleus ("inner blobs," Fig. 11*b*). All features are circumscribed by the western radio structure. Subsections of this western bubble had been detected by HAM and FS.

Decomposition of the emission-line profiles in the incomplete western bubble reveals many similarities with its eastern counterpart. As in the east, the high-velocity gas generally has [N II] λ6583/H$\alpha \gg 1$, and the profiles are often composites of two high-velocity "bubble" components and the "disk" component near systemic velocity. The velocity splitting of the bubble components is largest near the mid-axis of the western bubble, reaching ~ 1000 km s^{-1}. Combining the velocity splitting that is measured in the incomplete bubble with the velocity measurements in the inner blobs, it also appears that there is a tendency for the splitting to first increase with radius up to $R \approx 900$ pc, and then to decrease outward. However, in reverse symmetry to the eastern bubble, the *redshifted* velocities in the western bubble generally exceed those on the blueshifted side (sometimes by as much as a factor of 3). This is consistent with the flow model presented in § 4.3.

4.8. *Line Splitting in the Inner Galactic Disk*

Anomalous velocities are also observed north of the nucleus along the inner galactic disk (P.A. $\approx -10°$; Fig. 11*a*). Split lines are found out to a radius of $\sim 16"$ (1.3 kpc), but in a sector of width only $\sim 2"$–$3"$ (170–335 pc). The degree of line splitting varies smoothly with radius, first increasing monotonically to ~ 275 km s^{-1} at 200–300 pc radii, beyond which it decreases. It is interesting that [N II] λ6583/Hα = 0.5–2.0 in this region, with the blue-wing and red-wing components having similar ratios.

The smooth transition between the velocity field of the blue-wing component in the eastern bubble and the kinematics of the blue-wing component in the inner disk suggests a common dynamical origin. On the other hand, it is not clear whether the red-wing component in the disk is associated with the red-wing component of the bubble or with the galactic disk itself. Non-rotational velocities of the H_2 molecular gas were also detected near this region by Irwin & Sofue (1992).

5. DISCUSSION

A thorough investigation of the western bubble in NGC 3079 is impossible because it is so obscured by dust in the

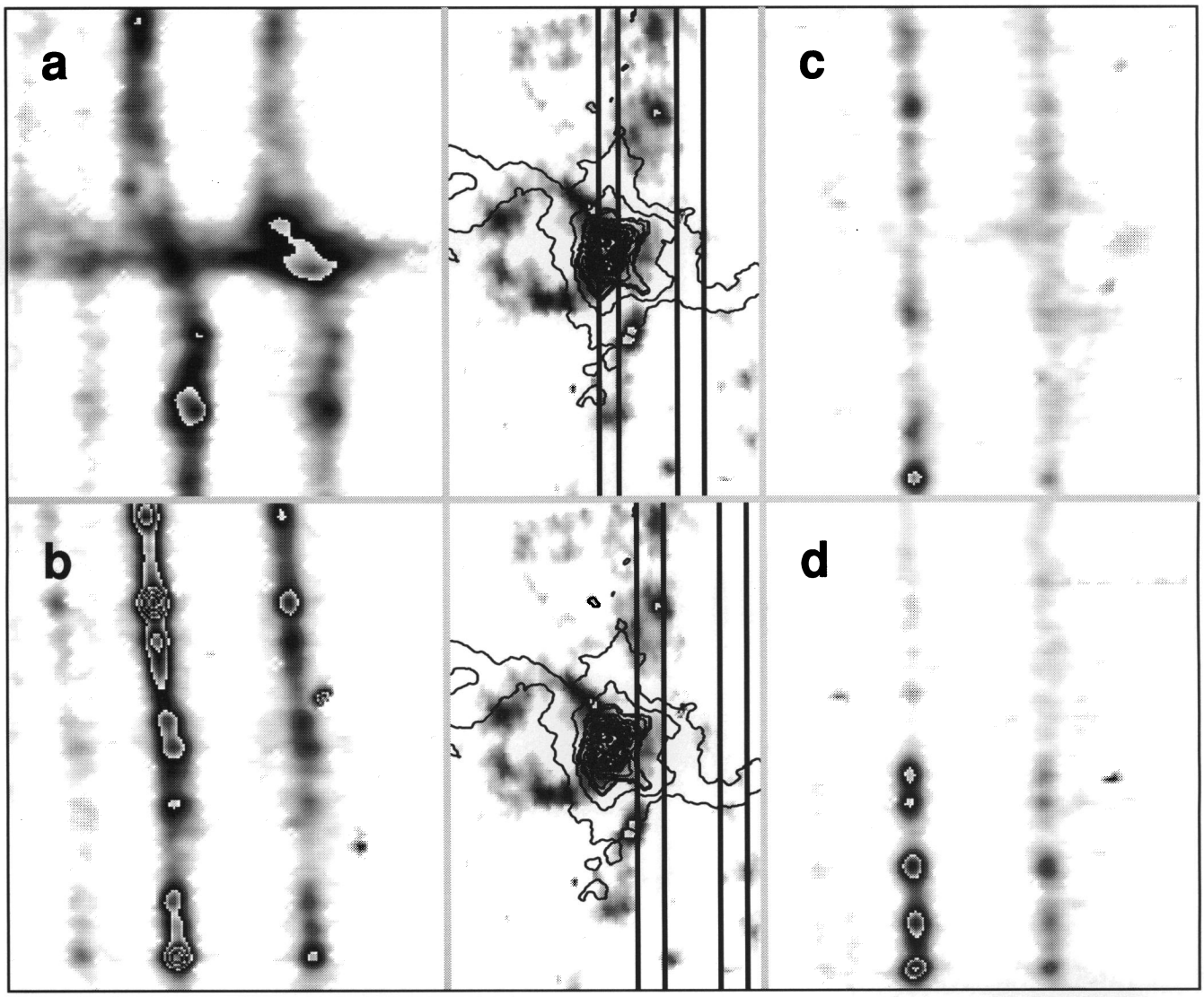

FIG. 11.—Anomalous velocities in the inner galactic disk and bubble. The presentation is the same as in Fig. 2 except that the "slit-width" is now 3.″5 in panels (*b*)–(*d*) and 2″ in (*a*). The data cube has been rotated so that the vertical slits run parallel to the major axis (−10° P.A.). Several contours from the 20 cm radio continuum map of Duric & Seaquist (1988) are shown for orientation. The offsets of the slit center from the nucleus are (*a*) 0.″5 W, (*b*) 5″ W, (*c*) 10″ W, and (*d*) 15″ W. Note the line splitting in the disk near the base of the bubble in (*a*), and the high-velocity gas at low flux levels in (*c*) and (*d*).

galaxy disk. The following will therefore focus on the dynamics and other physical properties of the eastern superbubble. However, it will be important to remember that the radio data of DS, the existence of an H I tail in NGC 3073 (Irwin et al. 1987; cf. § 5.4), and the results described in § 4.7 strongly suggest that the nuclear outflow in NGC 3079 is roughly symmetric with respect to the nucleus.

5.1. *Timescales*

The dynamical timescale of the superbubble can be estimated from the deprojected velocity of the entrained material, derived from our kinematic model (§ 4.3) and the linear dimensions of the bubble:

$$t_{\rm dyn} \approx 1 \times 10^6 R_{\rm bubble,\,kpc}\, V^{-1}_{\rm bubble,\,1000}\ {\rm yr}\ , \qquad (1)$$

where $V_{\rm bubble,\,1000}$ and $R_{\rm bubble,\,kpc}$ are in units of 1000 km s^{-1} and kpc, respectively. This timescale is comparable to that derived by DS from their wind model.

A second age can be estimated if the bubble has not reached blowout and can be approximated as an adiabatic structure with a radiative shell that expands through a uniform medium (Koo & McKee 1992a). Then the radius and expansion velocity of the shell are (CMW; Weaver et al. 1977)

$$R_{\rm bubble} = n_0^{-1/5} L^{1/5}_{w,44}\, t^{3/5}_{\rm bubble,6}\ \ {\rm kpc}\ , \qquad (2)$$

and

$$V_{\rm bubble} = 620 n_0^{-1/5} L^{1/5}_{w,44}\, t^{-2/5}_{\rm bubble,6}\ \ {\rm km\ s^{-1}}\ . \qquad (3)$$

Here $t_{\rm bubble,6}$ is the bubble age in Myr, n_0 is the ambient density in cm^{-3}, and $L_{w,44}$ is the kinetic/mechanical luminosity of the wind in units of 10^{44} ergs s^{-1} [$L_w = (\gamma - 1)\dot{M}_w c^2 \approx 1/2 \dot{M}_w V_w^2$, where $\dot{M}_w$ is the mass flux in the wind, V_w is the wind velocity, and γ is the associated Lorentz factor]. From equations (2) and (3) we find that

$$t_{\rm bubble} = 6 \times 10^5 R_{\rm bubble,\,kpc}\, V^{-1}_{\rm bubble,\,1000}\ \ {\rm yr}\ , \qquad (4)$$

a value very similar to the dynamical age. Using the cooling function of Gaetz & Salpeter (1983) and assuming $T_e \approx 10^{7-8}$ K, $N_e \approx 1$ cm^{-3} in the wind (e.g., Chevalier & Clegg 1985), we obtain a cooling time for the wind gas of $\sim 10^{7-8}$ yr, considerably larger than the dynamical age of the bubble. The assumption of adiabaticity in the bubble is thus reasonable—radiative cooling of the hot wind material is probably not important in the dynamical evolution of the bubble (cf. MM). On the other hand, we will argue in § 5.4 that the bubble may be blown out. The timescale derived from equation (4) should thus be used with caution.

The possibility of inflating the bubble by injecting kinetic energy from intense circumnuclear star formation will be discussed in § 5.5. It is therefore useful to compare the dynamical age of the bubble with the age of the starburst and the time to deplete gas in the starburst. In this scenario, the IR luminosity measures the total stellar luminosity, so it can be used to find the rate of star formation. From the derivations of Gallagher, Hunter, & Tutukov (1984) and Hunter et al. (1986) we have

$$SFR({\rm IR}) = 26 \beta^{-1} L_{\rm ir,\,11}\ M_\odot\ {\rm yr}^{-1} \qquad (5)$$

where the IR luminosity is in units of 10^{11} $L_\odot$ and β is the fraction of the bolometric luminosity radiated by stars. This assumes that the star-formation rate is constant over the lifetime of stars with $M \geq 10$ $M_\odot$ and that the initial mass function (IMF) extends up to ~ 100 $M_\odot$ with slope $\gamma = 2.35$ (Salpeter 1955). Using the IR luminosity measured by Soifer et al. (1987; adjusted to a distance of 17.3 Mpc), the star-formation rate in NGC 3079 is roughly $10\beta^{-1}$ $M_\odot$ yr. Note that this includes a (probably large) contribution from the disk (cf. § 5.3), and is therefore an upper limit to the nuclear rate. Combining this star formation rate with the total mass of atomic and molecular gas observed in the galaxy *core* (Irwin & Seaquist 1991), we derive a depletion time of $\gtrsim 10^9 \beta$ yr.

The age of the starburst is harder to constrain. We can compare the optical spectrum of the nucleus with the predictions of the starburst models of Bica, Alloin, & Schmidt (1990). We find that the strength of the Balmer absorption in the nuclear spectrum (see, for instance, Fig. 1 of FS) is consistent with a starburst age greater than 10^7 yr, similar to those found by Rieke et al. (1980, 1985) in several classical starburst galaxies.

In summary, we find that both the starburst age and the depletion time of the gas through star formation are considerably longer than the age of the bubble. Therefore, these timescale arguments are consistent with the possibility that the starburst is driving the bubble expansion.

5.2. *Ionized Masses*

Table 3 shows the integrated Hα luminosities and [N II] λλ6548, 6583/Hα ratios across the bubble for each component. The dereddened quantities were derived using conservatively small extinction: $\tau({\rm H}\alpha) = 1$ when the vertical height with respect to the plane of the disk is smaller than 4″ and $\tau({\rm H}\alpha) = 0$ elsewhere (§ 4.5). If the gas with density N_e is in Case B recombination conditions at 10^4 K, the ionized masses are $\sim 5 \times 10^6 N_e^{-1}$ $M_\odot$ for each component. Shocks, if present in the bubble (§ 4.6 and § 5.6), will not significantly alter these masses because most of the Hα emission is still produced by recombination rather than by collisional excitation (e.g., Shull & McKee 1979; BDT). Our constraints on the average gas density ($\lesssim 125$ cm^{-3}, see § 4.4) yields a total ionized mass in the blueshifted and redshifted bubble components of $\gtrsim 1 \times 10^5$ $M_\odot$, a mass similar to that involved in the well-known outflows in the starburst galaxy M82 ($\sim 2 \times 10^5$ $M_\odot$; Bland & Tully 1988; HAM) and the Seyfert galaxy NGC 1068 ($\sim 2 \times 10^5$ $M_\odot$; Cecil, Bland, & Tully 1990).

This mass can be compared with the total mass of ambient ISM available in the cylinder of height $H \approx 1$ kpc and radius $R_{\rm bubble} \approx 1$ kpc. Using the H I disk parameters of Irwin & Seaquist (1991), we get $M_{\rm ISM} \approx$ a few 10^6 $M_\odot$. This value is probably an underestimate of the actual mass because it does not include the contribution from the molecular disk. The windblown bubble models of MMN show that $\sim 7.5\%$ of the total ISM mass in this cylinder is injected into the halo as cold clouds. If these models apply to NGC 3079, the superbubble is therefore likely to be mostly disk material.

The rate of mass outflow can be estimated if it has been constant over the dynamical age of the bubble:

$$\frac{dM}{dt} \simeq \frac{M_{\rm bubble}}{t_{\rm dyn}} = 10 M_{\rm bubble,\,7}\, V_{\rm bubble,\,1000}\, R^{-1}_{\rm bubble,\,kpc}$$
$$\gtrsim 10 N_e^{-1}\ M_\odot\ {\rm yr}^{-1}\ , \qquad (6)$$

where in principle $M_{\rm bubble,\,7}$ is the sum of the wind and entrained gas in the outflow (which does not include the "disk" component) in units of 10^7 $M_\odot$. However, the value given in equation (6) is a lower limit because it accounts for

only the ionized entrained mass. Using their radio data, DS estimated the mass outflow rate *in the wind* to be $\sim 7\ M_\odot\ \mathrm{yr}^{-1}$ (for $D = 17.3$ Mpc).

We will argue in § 5.4 that the superbubble is probably blowing out of the galaxy disk. So, most of the outflow mass is being deposited in the galactic halo or escaping from the galaxy. Both the wind and, to a lesser extent, the entrained mass are likely to be enriched in metals by the nuclear starburst or AGN (cf. §§ 4.5 and 5.5.1; Maeder 1990; Guessoum & Gould 1989). For example, the models of Maeder (1990) predict mass fractions for the metals as large as 25% in the starburst-driven wind. If all the wind mass remains bound to the galaxy, we find that this component alone can contribute up to $5t_{\mathrm{outflow},8}$% of the total metal content of the galaxy, where $t_{\mathrm{outflow},8}$ is the outflow lifetime in units of 10^8 yr. (We assume a total mass for NGC 3079 of $\sim 2 \times 10^{11}\ M_\odot$ [Irwin & Seaquist 1991, corrected for our adopted distance of 17.3 Mpc] and solar metal abundance, averaged over the whole galaxy.) Contributions from the entrained material will add to this. The nuclear outflow may therefore be an important source of metals in NGC 3079.

5.3. *Energies and Momenta*

The bulk kinetic energies listed in Table 3 were calculated by summing the quantity $M_j V_j^2$ at each spatial element j across the superbubble, where M_j corresponds to the mass of ionized gas found from the Hα flux at location j and the value of V_j is found from the radial velocity law that best fits the data. Similarly, the integrated momentum of each component is found by summing the $M_j V_j$ contributions. In Table 3, the "turbulent" kinetic energy represents the spatially unresolved kinematic substructure derived from the observed line widths: $\Sigma_j M_j \sigma_j^2$ where $\sigma_j = \mathrm{FWHM}_j/1.67$.

All quantities are scaled by the average gas density, constrained from the [S II] ratio measurements to be less than 125 cm^{-3} (§ 4.4). For this exercise, we adopted an egg-shaped bubble with $i = 2°.5$, $n = 2.5$ and $V(1\ \mathrm{kpc}) = 3600\ \mathrm{km\ s}^{-1}$. In this model, about 40% of the bulk kinetic energy and 60% of the momentum originate in the lower half of the bubble. *Therefore, uncertainties in the geometry of the outflow in the upper half of the bubble (where projection effects are most important) can overestimate the quantities tabulated by factors of at most 2–3.* Indeed, the scenario in which the negative velocity gradient near the top of the bubble is produced by deceleration of the entrained gas rather than projection effects (cf. § 4.3) results in bulk kinetic energies and momenta only 30% smaller than those tabulated. Similarly, the discrepancies off-axis between our model and the data (Fig. 8) do not significantly affect our results. The total kinetic energy in the outflow of NGC 3079 ($\sim 2 \times 10^{56} N_e^{-1}$ ergs) may be 10 times the kinetic energies of the outflows in M82 ($\lesssim 2 \times 10^{53}$ ergs; Bland & Tully 1988; HAM) and NGC 1068 ($\sim 4 \times 10^{53}$ ergs; Cecil, Bland, & Tully 1990).

Following the same reasoning as in § 5.2, the rate of kinetic energy injected into the outflow is approximately:

$$\frac{dE_{\mathrm{kin}}}{dt} \simeq \frac{E_{\mathrm{kin}}}{t_{\mathrm{dyn}}} = 3 \times 10^{42} E_{\mathrm{kin},56}\, V_{\mathrm{bubble},1000}\, R_{\mathrm{bubble,kpc}}^{-1}$$

$$\approx 6 \times 10^{42} N_e^{-1}\ \mathrm{ergs\ s}^{-1}\ . \quad (7)$$

The input rate of kinetic energy in equation (7) is a lower limit to the total input rate of energy required to inflate the bubble because it ignores the contributions of the entrained neutral component and the wind material, and because a conservatively small reddening correction was applied to the energies in Table 3. Nor does this rate include the contribution from the outflow on the west side of the nucleus (cf. § 4.7).

The mechanical luminosity of the wind can also be estimated from equations (2) and (3):

$$L_{w,44} = 3 R_{\mathrm{bubble,kpc}}^2\, V_{\mathrm{bubble},1000}^3\, n_0\ \mathrm{ergs\ s}^{-1}\ , \quad (8)$$

where n_0 is the ambient density of the ISM in cm^{-3}. For comparison, DS derived from their radio data an energy flow rate *for the wind* of 7×10^{43} ergs s^{-1} (for our adopted distance of 17.3 Mpc).

Similarly, the input momentum rate in this outflow is approximately

$$\frac{dp_{\mathrm{kin}}}{dt} \simeq \frac{p_{\mathrm{kin}}}{t_{\mathrm{dyn}}} = 3 \times 10^{34} p_{\mathrm{kin},48}\, V_{\mathrm{bubble},1000}\, R_{\mathrm{bubble,kpc}}^{-1}$$

$$\gtrsim 8 \times 10^{34} N_e^{-1}\ \mathrm{dyn}\ , \quad (9)$$

while an adiabatic bubble enveloped by a radiative shell in the pre-blowout phase has a wind momentum input rate of

$$\frac{dp_w}{dt} = 2 \times 10^{36} R_{\mathrm{bubble,kpc}}^2\, V_{\mathrm{bubble},1000}^2\, n_0\ \mathrm{dyn}\ . \quad (10)$$

In contrast, a wind momentum input rate ($dp_w/dt = \dot{M}_w V_w$) of 3×10^{35} dyn was derived by DS based on their model ($D = 17.3$ Mpc).

Lower limits on the densities may be derived from dynamical arguments. The upper limit to the density derived from the [S II] ratio implies that the gas pressure in the emission-line gas is less than $\sim 3.5 \times 10^{-10}$ dyn cm^{-2} (we assumed $T_e \approx 10^4$ K). This can be compared to either the ram pressure of the wind (for a ruptured bubble) or to the thermal pressure in the

TABLE 3

CHARACTERISTICS OF THE OUTFLOW

Component	Hα Luminosity[a]				Case B Recombination[b]		
	Observed (10^{39} ergs s^{-1})	Dereddened[c] (10^{39} ergs s^{-1})	[N II] (6548 + 6583)/Hα	Mass ($10^6\ M_\odot/n_e$)	E_{Bulk}[d] ($10^{56}/n_e$ ergs)	$E_{\mathrm{turbulent}}$ ($10^{54}/n_e$ ergs)	Momentum[d] ($10^{48}/n_e$ dyn s^{-1})
Blue wing	0.69	1.4	4.1	4.7	1.0	3.1	1.1
"Disk"	1.4	2.7	0.9	8.8	...	0.84	...
Red wing	0.81	1.8	2.4	5.9	0.88	4.1	1.3

[a] The adopted distance of NGC 3079 is 17.3 Mpc (Tully et al. 1992).
[b] For Case B recombination at $T \approx 10^4$ K.
[c] Dereddened values using a dust optical depth $\tau(\mathrm{H}\alpha) = 1$ within 4″ above the galactic disk.
[d] Assuming an egg-shaped bubble with $i = 2°.5$, $n = 2.5$, and $V(1\ \mathrm{kpc}) = 3600\ \mathrm{km\ s}^{-1}$.

shocked wind material inside the bubble (when the bubble has not blown out). In the first case, the momentum flux is simply the upper limit to the pressure given above multiplied by the surface area of the bubble. We obtain $dp/dt \lesssim 1.3 \times 10^{34}$ dyn. Comparing this number with the result of equation (9), we derive $N_e \gtrsim 10$ cm^{-3}. In the case of a confined bubble, the thermal pressure is two-thirds of the energy density and the energy density is roughly equal to the time-integrated kinetic energy input divided by the volume of the bubble. This estimate has to be corrected downward by a factor 5/11 for an adiabatic bubble, and then corrected upward by the ratio of the entire bubble volume to the volume occupied by the shocked wind material. Ignoring these two factors for simplicity (because they will roughly cancel each other out) and taking a dynamical age of 1×10^6 years for the bubble (eq. [1]), we then find that the predicted thermal pressure in a confined bubble is 1.5×10^{-9} dyn cm^{-2} if $dE/dt = 1 \times 10^{42}$ ergs s^{-1}. Consequently, for the predicted thermal pressure to be consistent with the measured upper limit, dE/dt must be less than 2.3×10^{41} ergs s^{-1} or, according to equation (7), $N_e \gtrsim 30$ cm^{-3}. We will argue in the next section that the case of a ruptured bubble is more likely to apply to the superbubble of NGC 3079.

5.4. *Dynamical State of the Superbubble*

Before discussing the energy source of the outflow, it is important to establish the evolutionary phase of the superbubble. In this context, the crucial question is whether the superbubble has blown out of the galactic disk. Despite the apparent closed morphology of the line-emitting bubble at low intensity levels (cf. Fig. 1), many characteristics of the outflow in NGC 3079 suggest that the bubble is at least partially blown out:

1. Numerical studies of bubble growth in various stratified atmospheres predict that blowout occurs where the bubble diameter is comparable to the scale height of the disk (e.g., Schiano 1985; MM; TI; MMN). The diameter of this bubble ($\sim$1.1 kpc) is considerably larger than the scale height of the molecular disk ($\sim$100 pc; e.g., Young, Claussen, & Scoville 1988), and is comparable to the scale height of the H I disk ($\sim$1 kpc; Irwin & Seaquist 1991). In the nomenclature of Heiles (1990) this superbubble is therefore a "breakthrough bubble" and possibly even a "blowout bubble."

2. The previous argument can be quantified by using the blowout criterion of MM and MMN (see also Schiano 1985 and Koo & McKee 1992a):

$$D \simeq 3.0 \times 10^{-42} (dE/dt) H_{\rm kpc}^{-2} P_7^{-3/2} n_0^{1/2} > 100 , \qquad (11)$$

where dE/dt is the input energy rate in the bubble, $H_{\rm kpc}$ is the scale height of the galactic disk in kpc, and P_7 is the ambient pressure, P/k, in units of 10^7 K cm^{-3}. Using conservative estimates for the disk parameters ($H_{\rm kpc} \approx 1$, $n_0 \approx 1$, and $P_7 \approx 0.01$), we find that the bubble is blown out of the H I disk if $dE/dt \gtrsim 3 \times 10^{40}$ ergs s^{-1}. The input rate of kinetic energy calculated in the previous section with equation (7)—a lower limit to the actual input energy rate in the bubble—satisfies this condition. As we will briefly discuss in § 5.8, the presence of a magnetic field in the bubble will alter the blowout condition used in the present discussion by increasing the critical input rate needed for blowout.

3. The kinematic model that best fits our data implies that the velocity of the line-emitting gas at the boundary of the optical bubble increases approximately with the square of the distance from the nucleus (§ 4.3). Such a steep velocity gradient is not observed in numerical simulations of pre-blowout bubbles, but is more characteristic of the blowout of free-wind phases (e.g., Schiano 1985; Tenorio-Tagle et al. 1987; MM; MMN; Koo & McKee 1992a). Moreover, the success of the model with radial motions from the nucleus suggests that the outflow has not been strongly thermalized by its passage through the bubble to its boundary.

4. The split emission lines in the inner galactic disk (§ 4.8) strongly suggest that the outflow extends beyond the bubble boundary.

5. The radio emission mapped by DS lies outside the line-emitting bubble (cf. Fig. 1). DS suggested that the synchrotron-emitting relativistic electrons in this region have broken through the bubble and are interacting with the ambient ISM. This displacement suggests blowout. Alternatively, these relativistic electrons may be produced by particle reacceleration across the shocked bubble boundary (§ 5.6).

6. Another argument for a free wind is the presence of an elongated H I plume in the companion galaxy NGC 3073, which is remarkably well aligned with the nucleus of NGC 3079 (Irwin et al. 1987). Irwin et al. have argued convincingly that this plume results from ram pressure stripping by an outflowing wind from NGC 3079. The detection by FS of starburst activity in NGC 3073 further supports this scenario. A comparison of the dynamical age of the bubble with the travel time to NGC 3073 suggest that the relativistic component of the wind decouples from the thermal component beyond the shell (DS). An excellent test of this hypothesis would be the detection of a steep gradient in the thermal wind density ($\sim R^{-2}$).

7. The X-ray emission in NGC 3079 is spatially resolved, extending up to $\sim$2′ in the same direction as the emission-line bubble (Fabbiano, Kim, & Trinchieri 1992; Reichert, Mushotzky, & Filippenko 1994). This morphology suggests that some X-rays are produced by a hot plasma *outside* the optical bubble boundary. X-ray emission outside windblown bubbles is not expected before their blowout (cf. § 5.8).

Some cautionary remarks are necessary. Comparison between the observations and numerical simulations of windblown bubbles should be considered only illustrative because some models predict shell velocities less than 10% those observed in NGC 3079. An important distinction should be made between blown out and ruptured bubbles. A blown out bubble is not necessarily ruptured because the growth time of Rayleigh-Taylor instabilities may be 10^7 yr (e.g., Koo & McKee 1992a). Arguments (1) and (2) suggest that the bubble is in the blowout phase, while arguments (3)–(7) suggest that the bubble is at least partially ruptured and that hot, shocked wind gas is escaping beyond its boundaries. Note, however, that the evidence for a ruptured bubble can be explained by positing intermittent activity in NGC 3079. In this scenario, the optical bubble is produced by a recent outflow event that is physically unrelated to the outer and older free-flowing components (cf. DS). As TI have noted, the X-ray flux profile may help to discriminate between continuous and impulsive energy injections, and the X-ray data discussed in § 5.7 appear more consistent with the first scenario.

To summarize, the superbubble in NGC 3079 is likely to be blown out and may also be partially ruptured. An important consequence is that the formalism of CMW, Weaver et al. (1977), MM, MMN, and HAM derived for bubbles in the snowplow phase is not rigorously applicable to this outflow.

The results derived in this paper from equations (2), (3), (4), (8), and (10) should therefore be considered order-of-magnitude estimates.

5.5. *Energy Source of the Superbubble: Starburst or AGN?*

5.5.1. *Evidence for a Nuclear Starburst and an Active Nucleus in NGC 3079*

Several observations point to the presence of a nuclear starburst in the core of NGC 3079. Lawrence et al. (1985) find an extended 10 μm source and a color excess at 10 and 20 μm that they interpret as emission from strongly heated dust. Other evidence for large quantities of dust in the nuclear region comes from the presence of a molecular disk with radius ~ 1 kpc, total thickness ~ 200 pc, and an H_2 mass of 1.3×10^{10} $M_\odot$ ($\sim 50\%$–60% of the total dynamical mass in the nuclear disk; Irwin & Sofue 1992). Most of the clouds in this disk are aligned with the plane of the galaxy disk and rotate about the nucleus. Combining the IR luminosity derived from the *IRAS* fluxes with the total H_2 mass of NGC 3079, we find that $L_{ir}/M_{H_2} \approx 3\ L_\odot/M_\odot$, a value very similar to the value of 3–4 $L_\odot/M_\odot$ for the Milky Way (Scoville & Good 1986). Although higher resolution IR maps are needed to learn whether L_{ir}/M_{H_2} varies with position from the nucleus, the IR radiation is naturally explained by molecular clouds undergoing star formation with Galactic efficiency. The presence of a powerful H_2O maser (Henkel et al. 1984; Haschick & Baan 1985; Haschick et al. 1990) also suggests intense star formation in the core.

The evidence for an AGN in NGC 3079 is weaker and comes mainly from the high-resolution radio continuum observations of DS and Irwin & Seaquist (1988). DS found that the radio power from the nucleus ($R \lesssim 15$ pc) at 4866 MHz is $\sim 10^{22}$ W Hz^{-1}. The spectrum is slightly inverted with $\alpha = +0.15$ ($S_\nu \propto \nu^\alpha$). As DS note, the brightness and the inverted spectrum are very unusual for the core of a spiral galaxy, and are more typical of radio galaxies and quasars. VLBI observations by Irwin & Seaquist (1988) show three roughly coaligned components within the central parsec. Irwin & Seaquist (1988) argue that the positions, sizes, and fluxes of these components suggest a jet outflow from a central compact object rather than radio supernovae from a starburst.

Indeed, as discussed extensively by Irwin & Seaquist, the VLBI components would be among the most luminous radio supernovae yet detected and would be similar in radio brightness and linear size to the unique SN 1979C discovered in M100 by Weiler et al. (1983). Three ultraluminous supernovae would have had to occur nearly simultaneously within 1 pc of each other, close to the kinematic center of the galaxy, and without supernovae of comparable luminosity nearby. The implied supernova rate would be 0.5 yr^{-1} pc^{-3}! The radio supernova scenario also has difficulty explaining the preferred alignment between the various VLBI sources, and the lack of a noticeable decrease in the flux density over the 10 or so years since this object was first mapped in the radio.

Irwin & Seaquist (1988) suggest that the nuclear radio jet is also responsible for the outer radio lobes (DS; Fig. 1). Misalignment between the pc-scale jet (P.A. $\simeq 125°$) and the kpc-scale structure (P.A. $\simeq 60°$) is explained either through buoyancy effects caused by the pressure gradient in the galactic disk or by the ram pressure of the rotating ISM.

5.5.2. *Morphological Argument*

A qualitative argument in favor of an AGN origin to the outflow follows from the morphology of the superbubble. Our data show that the bubble apex near the nucleus is pointed, with a lateral extent of only $\sim 2''$–$3''$. This should be compared to the size of the nuclear starburst, $\sim 10''$–$20''$ (§ 5.5.1). A bubble with a pointed apex is a natural consequence of a point energy such as an AGN. However, the considerable quantity of dust near the nucleus of NGC 3079 may distort the optical morphology of the bubble near the energy source, weakening this morphological argument. Moreover, it is possible that the energy which is used to inflate the bubble originates solely from the more active, nuclear portion of the starburst (cf. § 5.5.3).

5.5.3. *Dynamical Argument*

The question we address in this section is whether the observed nuclear starburst in the core of NGC 3079 has the energy to power the superbubble. In § 5.3 we estimate the input rate of kinetic energy in the entrained gas to be *at least* $\sim 6 \times 10^{42} N_e^{-1}$ ergs s^{-1} (10 cm$^{-3} \lesssim N_e \lesssim 125$ cm^{-3}), assuming a constant rate over the dynamical age of the bubble. This rate can be compared with the injection rate *predicted* by the starburst scenario. In the starburst model, both stellar winds and supernovae are contributing to the kinetic energy of the bubble. The injection rate of this kinetic energy into the ISM is related to the star formation rate through the slope of the IMF and its upper mass limit. Using the calculations of Elson, Fall, & Freeman (1989; see also HAM) to translate the star-formation rate derived from equation (5) into the kinetic energy injection rate, we obtain

$$\frac{dE_*}{dt} = 7 \times 10^{42} f_{nuc} L_{ir,11} \text{ ergs s}^{-1} \approx 3 \times 10^{42} f_{nuc} \text{ ergs s}^{-1} . \quad (12)$$

The IR luminosity that we used in this calculation (Soifer et al. 1987) includes that of the galaxy disk. The factor f_{nuc} is the fraction of the infrared luminosity produced in the nucleus ($R \lesssim 3'' \approx$ the lateral extent of the bubble apex). This quantity can be estimated from the ground-based observations of Willner et al. (1985), Lawrence et al. (1985), Devereux (1987), and Armus (1994). They found that about 10% of the 10–12 μm emission comes from the inner 5″. Thus, unless the spectral energy distribution of the nucleus is significantly different from that in the outskirts of the galaxy, f_{nuc} is likely to be ~ 0.1 and $dE_*/dt \approx 3 \times 10^{41}$ ergs s^{-1}. The present injection rate of the nuclear starburst therefore appears sufficient to power the observed outflow if $N_e \gtrsim 20$ cm^{-3}. This lower limit on the density is within the acceptable range determined from our measurements of the [S II] ratio (§ 4.4) and from dynamical arguments (§ 5.3): 10 cm$^{-3} \lesssim N_e \lesssim 125$ cm^{-3}.

If radiative losses are important the input kinetic energy is not conserved, but the bubble may still conserve momentum. Then, the observed momentum injection rate (eq. [9]) should be compared with the predictions of the starburst scenario (Elson et al. 1989):

$$\frac{dp_*}{dt} = 6 \times 10^{34} f_{nuc} L_{ir,11} \text{ dyn} \approx 2 \times 10^{33} \text{ dyn} . \quad (13)$$

This rate requires $N_e \gtrsim 40$ cm^{-1} to explain the value derived from our spectra (eq. [9]). Once again, the nuclear starburst of NGC 3079 appears strong enough to power the superbubble without the help of another source of energy such as an AGN. In this scenario, the starburst *outside* of the nuclear region may

have been triggered by the expanding bubble-shock that propagates through the galaxy disk (Schiano 1985; McCray & Kafatos 1987; Tenorio-Tagle & Palous 1987; MMN; TI; Norman & Ikeuchi 1989; Palous, Franco, & Tenorio-Tagle 1990; cf. § 4.8).

The possibility that the putative AGN in the core of this galaxy drives some of the outflow cannot be completely excluded from our data. But its exact importance depends critically on the density of the entrained material. It also depends on the kinematic contribution of the entrained neutral gas and the wind, and the contribution of the outflow on the west side of the nucleus. These quantities will need to be better constrained to determine the exact importance of the AGN on the dynamics of the superbubble. In the pure black hole scenario, a small mass of less than $\sim 10^3\ M_\odot$ can power the outflow for 10^6 yr if we assume 10% conversion efficiency.

5.6. *Importance of Shock Ionization*

In § 4.6, we argued that shock ionization is a likely source of ionization across the bubble, based on the emission-line ratios and the violent velocity field. However, we could not exclude an extended source with a hard continuum that photoionizes high-metallicity gas. Viegas-Aldrovandi & Contini (1989) have emphasized the importance of considering many emission lines to isolate the contribution of shock heating/ionization from the photoionization of a hard continuum. The few lines available to us are clearly insufficient. However, the relative importance of shock ionization may be constrained by comparing the observations with other predictions of shock models.

Shocks with velocity $V_s \approx 500$ km s^{-1} will heat the ISM to a temperature

$$T_s \approx 3.5 \times 10^6 (V_s/500)^2 \text{ K} , \quad (14)$$

yielding a cooling time to 10^4 K of

$$t_c \approx 3.2 \times 10^3 n_s^{-1} T_s^{1.5} \simeq 7 \times 10^5 n_s^{-1} (V_s/500)^3 \text{ yr} , \quad (15)$$

where n_s is the postshock density or four times the ambient proton density. The optical line emission will be produced once the gas cools to $\sim 10^4$ K. A planar shock front is displaced from the line-emitting gas by

$$l_c \approx t_c V_s \approx 88 n_0^{-1} (V_s/500)^4 \text{ pc} . \quad (16)$$

Note the strong dependence of the cooling length on the shock velocity. Taylor, Dyson, & Axon (1992) show that the dependence is $l_c \propto V_s^n$ with $n \approx 1$–2.2 when the geometry is nonplanar (e.g., for a bow shock.) Although shock velocities of ~ 750 km s^{-1} can explain the large displacement between the line-emitting bubble and part of the radio structure (Fig. 1), the postshock cooling time may exceed the bubble age (eq. [15]). In addition, the ionizing radiation from the AGN or starburst will heat the postshocked gas and increase the cooling length, as in the bow shock models of Taylor et al. (1992).

The total energy dissipated in the shock each second is

$$L_{\text{shock}} \simeq \tfrac{1}{2} \rho A V_s^3 = 7.9 \times 10^{27} n_a A V_s^3 \text{ ergs s}^{-1} , \quad (17)$$

where A is the shock surface area in pc^2. From BDT, we have

$$L(\text{H}\alpha)_{\text{shock}} \approx 3L(\text{H}\beta)_{\text{shock}} \approx 3L_{\text{shock}}/100 = 3 \times 10^{34} n_a A (V_s/500)^3 \text{ ergs s}^{-1} \quad (18)$$

if 90 km s^{-1} $< V_s <$ 1000 km s^{-1} and if thermal instabilities have no effect. The ambient (preshock) ISM density in this SBc galaxy is plausibly ~ 1 cm^{-3} and $A \lesssim 4\pi(550)^2 \approx 4 \times 10^6$ pc^2 (this is an upper limit because the bubble is not complete; § 4.3). The expected Hα luminosity of the shock is comparable to the dereddened Hα luminosity of the bubble components listed in Table 3 if $V_s \gtrsim 150$ km s^{-1}. The possible difference between the predicted shock velocity and the actual velocities of the entrained material ($\sim$500–1000 km s^{-1}) may indicate that the pre-shock medium was already in motion, perhaps the result of a previous outburst.

The rate at which ISM gas is shocked is simply $dM/dt_{\text{shock}} = \rho A V_s$, so equations (17) and (18) imply that

$$dM/dt_{\text{shock}} \approx 40 L_{\text{H}\alpha,40}\ M_\odot \text{ yr}^{-1} , \quad (19)$$

where the Hα luminosity is in units of 10^{40} ergs s^{-1}. Thus, to shock-excite the entire line-emitting bubble would require $dM/dt \approx 13\ M_\odot$ yr^{-1}, or the equivalent of $1 \times 10^7\ M_\odot$ of shocked gas over the dynamical age of the bubble. This mass corresponds to $\sim 0.1\%$ of the total amount of H_2 gas available in NGC 3079. Considering the large uncertainties on both the observed and predicted values, it seems physically possible to power most of the line emission across the bubble with shocks without the need to invoke photons from the nuclear source.

5.7. *X-Ray Properties*

X-rays can be emitted from three of the four zones described by CMW and Weaver et al. (1977): the thin shell of shocked ambient gas (zone C in the nomenclature of Weaver et al.), the shocked wind gas (zone B), and the wind itself (zone A). In addition, the nuclear source (AGN and/or starburst) will contribute. The X-ray emission from the free-flowing wind is likely to be only a minor contributor. Weymann et al. (1982) and Schiano (1985) have argued that the nuclear (nonthermal) X-ray emission from an AGN will generally dominate that of its wind. Moreover, the X-ray surface brightness of the free wind is expected to decrease rapidly with height above the galaxy disk plane, $\propto z^{-11/3}$ (TI), because of adiabatic cooling. In contrast, the predicted surface brightness of the shocked wind is nearly constant or even increases with height (cf. 12 in TI). The temperature and density in this region are approximately (CMW and Weaver et al. 1977)

$$T_{\text{X}} = 6 \times 10^7\, dE/dt_{43}^{8/35} n_0^{2/35} t_6^{-6/35} \text{ K} \quad (20)$$

and

$$n_{\text{X}} = 0.12\, dE/dt_{43}^{6/35} n_0^{19/35} t_6^{-22/35} \text{ cm}^{-3} , \quad (21)$$

where dE/dt is the mechanical energy input from the wind, n_0 is the density of the ambient material, and t_6 is the age of the bubble in Myr. Thus, the shocked wind will cool by free-free emission with luminosity

$$L_{\text{X}} = 7 \times 10^{39}\, dE/dt_{43}^{37/35} n_0^{18/35} t_6^{13/35} \text{ ergs s}^{-1} . \quad (22)$$

Using the kinetic energy rate (eq. [7]) as a lower limit to dE/dt, $t_6 \approx 1$ (eqs. [1] and [4]), and $n_0 \approx 1$ cm^{-3}, we obtain $T_{\text{X}} > 5 \times 10^7 N_e^{-8/35}$ K (equivalent to $5N_e^{-8/35}$ keV), $n_{\text{X}} > 0.1 N_e^{-6/35}$ cm^{-3}, and $L_{\text{X}} > 4 \times 10^{39} N_e^{-37/35}$ ergs s^{-1} for the shocked wind in NGC 3079. These values depend very weakly on n_0 but assume that the bubble has *not* blown out.

In NGC 3079, a large portion of the shocked ambient material has apparently cooled to a temperature low enough to emit most of its energy at optical frequencies (the emission-line bubble). However, we have argued in § 5.4 that the bubble is probably blown out and may be partially ruptured. Some shell fragments may have low enough density for the ram pressure

from the wind to drive internal shocks with velocities $\sim 10^3$ km s^{-1}, which would produce X-rays.

Einstein studies of NGC 3079 by Fabbiano et al. (1982) and by Fabbiano et al. (1992) measure an integrated X-ray flux in the 0.5–4.0 keV HRI band of 5.91×10^{-13} ergs s^{-1} cm^{-2}, corresponding to an X-ray luminosity of 2×10^{40} ergs s^{-1} for our adopted distance of 17.3 Mpc. Fabbiano et al. (1992) also find that the X-ray flux is extended to the NE, nearly perpendicular to the disk plane. Recent *ROSAT* PSPC spectral maps by Reichert et al. (1994) show that the X-ray emission consists of a point source, superposed on fainter emission that extends 2'.5 in roughly the same direction as the emission-line bubble and the north-east radio structure. Reichert et al. argue that the total spectrum is well described as the superposition of a simpler power law of photon index 1.6 and a Raymond-Smith plasma of temperature 0.4 keV. These results strongly suggest that the energy source that powers the outflow also produces the point X-ray source, and that the lower level extended emission probably originates in the postshock wind material or low-density fragments of the bubble or both. The low temperature derived by Reichert et al. (1994) appears to exclude shocked wind material as the dominant X-ray emitter because equation (20) would require $N_e \approx 4 \times 10^4$ cm^{-3}! X-ray maps of higher spatial and spectral resolution are needed to more tightly constrain the origin of the X-rays in this galaxy.

5.8. *Effects of Magnetic Fields*

Duric et al. (1983) estimate that the average magnetic field strength associated with the eastern radio lobe is ~ 20 μG, yielding a magnetic pressure of 1.6×10^{-11} dyn cm^{-2}. On the other hand, the pressure of the line-emitting gas in the bubble is $3\text{–}35 \times 10^{-11}$ dyn cm^{-2} if $T \approx 10^4$ K and 10 $cm^{-3} \lesssim N_e \lesssim$ 125 cm^{-3} in the thermal gas. Consequently, the effects of the magnetic field on the dynamics of the superbubble are probably not very important. Nevertheless, it is instructive to explore consequences of neglecting the presence of this magnetic field in the previous discussion.

The magnetic field detected by Duric et al. (1983) is parallel to the minor axis at the top of the lobe, and parallel to the major axis in the galaxy disk, near the nucleus. As DS note, the simplest interpretation of these patterns is that the magnetic field is tied to disk gas that has been ejected along the minor axis. Recent numerical simulations of magnetized bubbles (e.g., Tomisaka 1990; Ferrière et al. 1991; Slavin & Cox 1992; Mineshige et al. 1993) show that energy injection in a medium with a modest ambient magnetic field of $\sim 3\text{–}5$ μG produces considerably smaller hot, remnant bubbles than when the field is ignored. This cushioning effect of the magnetic field produces shells that are thicker (less compressed) than in the models of MM, MMN, and TI (see also Innes 1992). The shock velocities derived in the unmagnetized case will overestimate the actual values. Therefore, all quantities that scale with shock velocity, such as the temperature of the shocked wind (eq. [20]), are likely to be somewhat *overestimated.*

These results also imply that the application of the formulae derived for unmagnetized bubbles to the superbubble of NGC 3079 may slightly *underestimate* its energy. This is another reason why we consider the input rates of kinetic energy and momentum of the entrained gas derived from equations (7) and (9) to be more reliable than the wind values that can be derived from the analytical formulae of MM, MMM, and others (eqs. [8] and [10]).

5.9. *Implications for Unified Models of Active Galaxies*

The nuclear superbubble of NGC 3079 is one of the few cases where a high-velocity ($\gtrsim 1000$ km s^{-1}) outflow is close enough to spatially resolve the outflowing gas from the ground. We can speculate about its appearance if this system was more distant and seen more nearly face-on. Because most of the intervening disk material has presumably been scoured clear by the outflow along the bubble axis, this galaxy orientation would allow a more direct view of the central energy source that powers the superbubble. The emission lines integrated across the core and bubble would probably show profiles with broad wings that extend over 2000–3000 km s^{-1}, as observed in Seyfert 1 galaxies and other broad-line objects. In addition, the presence of hot massive stars (and their associated high-velocity wind) in the nuclear starburst is likely to be responsible for substantial UV resonance absorption lines with large widths ($\gtrsim 1000$ km s^{-1}). Given that the radio power at 4.866 GHz of the nucleus of NGC 3079 is comparable to the brightest radio cores of Seyfert galaxies and rivals the fainter radio galaxies and quasars, a more distant and face-on NGC 3079 might be identified as a low-energy counterpart of the powerful but generally radio-quiet broad-absorption-line QSOs (BALQSOs; Turnshek 1988). Detailed high-resolution studies of the closest BALQSOs would help to clarify the relationship between this class of objects and less active galaxies such as NGC 3079.

6. SUMMARY

Our dynamical study of the nuclear outflow of NGC 3079 is based on Fabry-Perot and long-slit spectra. The complete two-dimensional coverage of the Fabry-Perot spectra has allowed us to accurately derive the kinematics and gaseous excitation of the gas in the spectacular nuclear superbubble. The complex emission-line profiles are produced by three distinct components: the blue- and red-wing "bubble" components with approximately constant line widths of 350 km s^{-1}, and a "disk" component with near-systemic velocities and line widths of ~ 130 km s^{-1}. The velocity separation of the bubble components is largest near the mid-axis of the bubble, exceeding 1500 km s^{-1}. The blueshifted velocities generally exceed the redshifted velocities. The velocity and surface brightness of the bubble components are often inversely correlated, as in optically thin planetary nebulae. However, in contrast to planetary nebulae, the observed radial velocities in the superbubble of NGC 3079 increase monotonically with nuclear radius until about three quarters of the diameter of the bubble; the high-velocity gas disappears very rapidly beyond this point. The incomplete *western* bubble shows a remarkable reverse symmetry in the kinematics of the line-emitting gas relative to the eastern bubble.

The gaseous excitation in the superbubble is unusual. At most points the [N II] λ6583/Hα ratio is greater than 2.5, and [S II] $\lambda\lambda$6716, 6731/Hα, [O I] λ6300/Hα, and [O III] λ5007/Hβ have nearly constant values of 0.6–0.9, 0.1–0.2, and 2.5–5.0. The [N II]/Hα ratio of the individual components is strongly correlated with their surface brightness. Measurements of the emission-line Balmer decrement across the bubble show that the dust concentrates along the galaxy plane but also attenuates emission from the base of the bubble.

The morphology and kinematics of the line-emitting gas in the superbubble are those of an egg-shaped structure with one apex at the nucleus, and delineated by gas that is accelerated radially from the nucleus such that $V_{\rm outflow} \propto R^n$ with $2 \lesssim n \lesssim$

3. The observed asymmetry in the velocity splitting is explained if the whole structure is inclined by $\sim 3°$ from the plane of the sky, as expected for an outflow that is perpendicular to the galaxy disk. In this picture, the smaller radial velocities observed at the top of the bubble are due to projection effects rather than a rapid deceleration in the outflow. This simple model also explains qualitatively the kinematics of the line-emitting gas in the incomplete western bubble. Based on conservatively small reddening corrections, a total ionized mass and kinetic energy of $\sim 1 \times 10^7/N_e$ $M_\odot$ and $\sim 2 \times 10^{56}/N_e$ ergs, respectively, are involved in the eastern superbubble. An upper limit of ~ 125 cm^{-3} for the electron density is estimated from the [S II] $\lambda 6716/\lambda 6731$ ratio (in its low-density limit even near the nucleus.) On the other hand, dynamical arguments suggest that $N_e \gtrsim 10$ cm^{-3}. The ionized mass present in this superbubble is therefore comparable to that outflowing from the starburst galaxy M82 and the Seyfert galaxy NGC 1068, but the kinetic energy may be 10 times larger than in M82 and NGC 1068.

The nuclear starburst appears sufficiently powerful to drive most of the outflow. This conclusion is relatively insensitive to the exact geometry of the velocity field at the top of the bubble. However, our results do not exclude the possibility that a central AGN also contributes to the outflow. The dynamical importance of this AGN critically depends on the density of the entrained line-emitting material, which is currently poorly constrained. In particular, the absence of a [S II] density gradient means that it cannot be used to find the size of the energy injection zone in this galaxy. Comparisons of the excitation properties of the line-emitting gas in this superbubble with the predictions of shock models suggest that shocks are responsible for most of its ionization.

Morphological and dynamical arguments imply that this superbubble is probably blowing out of the disk and is partially ruptured. The outflow ejects gas from the galactic disk into the halo and beyond at a rate greater than $10N_e^{-1}$ $M_\odot$ yr^{-1}. Part of this outflow is probably metal-enriched by the intense nucleosynthesis of the nuclear starburst or the AGN itself. The nuclear outflow may therefore be an important contributor to the metal enrichment of the galactic halo of NGC 3079 and the intergalactic medium. In a companion paper (Veilleux et al. 1994a) we investigate the consequences of this violent outflow on the galactic disk.

The radio maps used in this study were generously provided by N. Duric. L. C. Ho provided some assistance with data transfer. We thank R. C. Kennicutt and the referee, T. M. Heckman, for constructive comments on the manuscript. The flux calibration of the Fabry-Perot data was confirmed using numbers provided by T. M. Heckman, W. C. Keel, and J. S. Young. We are grateful for support of this research by NSF grants to the Universities of California (AST 89-57063), Hawaii (AST 88-18900), and North Carolina (AST 90-22128). S. V. gratefully acknowledges the financial support of the Natural Sciences and Engineering Research Council of Canada, and NASA through grant number HF-1039.01-92A awarded by the Space Telescope Science Institute that is operated by the AURA, Inc., for NASA under contract No. NAS 5-26555. J. B. H. acknowledges partial support from the Fullam award of the Dudley Observatory.

REFERENCES

Armus, L. 1994, private communication
Baldwin, J. A., Phillips, M. M., & Terlevich, R. 1981, PASP, 93, 5 (BPT)
Bica, E., Alloin, D., & Schmidt, A. 1990, MNRAS, 242, 241
Binette, L. 1985, A&A, 143, 334
Binette, L., Dopita, M. A., & Tuohy, I. R. 1985, ApJ, 297, 476 (BDT)
Bland, J., & Tully, R. B. 1988, Nature, 334, 43
———. 1989, AJ, 98, 723
Bland-Hawthorn, J., Shopbell, P. L., & Veilleux, S. 1994, in preparation
Brand, P. W. J. L., & Zealey, W. J. 1975, A&A, 38, 363
Burstein, D., & Heiles, C. 1978, ApJ, 225, 40
———. 1984, ApJS, 54, 33
Cardelli, J. A., Clayton, G. C., & Mathis, J. S. 1989, ApJ, 345, 245
Carozzi, N. 1977, A&A, 55, 261
Castor, R., McCray, R., & Weaver, R. 1975, ApJ, 200, L107 (CMW)
Cecil, G. N., Bland, J., & Tully, R. B. 1990, ApJ, 355, 70
César, M. L., Aldrovandi, S. M. V., & Gruenwald, R. B. 1985, PASP, 97, 850
Chevalier, R. A., & Clegg, A. W. 1985, Nature, 317, 44
de Bruyn, A. G. 1977, A&A, 58, 221
de Vaucouleurs, G., de Vaucouleurs, A. Corwin, H. G., Jr., Buta, R. J., Paturel, G., & Fouqué, P. 1991, Third Reference Catalogue of Bright Galaxies (New York: Springer)
Devereux, N. 1987, ApJ, 323, 91
Donahue, M., & Voit, G. M. 1991, ApJ, 381, 361
Dopita, M. A. 1994, in ASP Conf. Ser., The Physics of Active Galaxies, 287
Duric, N., & Seaquist, E. R. 1988, ApJ, 326, 574 (DS)
Duric, N., Seaquist, E. R., Crane, P. C., Bignell, R. C., & Davis, L. E. 1983, ApJ, 273, L11
Elson, R. A. W., Fall, S. M., & Freeman, K. C. 1989, ApJ, 336, 734
Fabbiano, G., Feigelson, E., & Zamorani, G. 1982, ApJ, 256, 297
Fabbiano, G., Kim, D.-W., & Trinchieri, G. 1992, ApJS, 80, 531
Ferland, G., & Mushotzky, R. F. 1984, ApJ, 264, 105
Ferland, G. J., & Netzer, H. 1983, ApJ, 264, 105
Ferrière, K. M., Mac Low, M.-M., & Zweibel, E. G. 1991, ApJ, 375, 239
Field, G. B. 1965, ApJ, 142, 531
Filippenko, A. V. 1985, ApJ, 289, 475
Filippenko, A. V., & Halpern, J. P. 1984, ApJ, 285, 458
Filippenko, A. V., & Sargent, W. L. W. 1988, ApJ, 324, 134
———. 1992, AJ, 103, 28 (FS)
Filippenko, A. V., & Terlevich, R. 1992, ApJ, 297, L79
Ford, H. C., Dahari, O., Jacoby, G. H., Crane, P. C., & Ciardullo, R. 1986, ApJ, 311, L7
Gaetz, T. J., & Salpeter, E. E. 1983, ApJS, 52, 155
Gallagher, J. S., Hunter, D. A., & Tutukov, A. V. 1984, ApJ, 284, 544
Goodrich, R. W., & Veilleux, S. 1988, PASP, 100, 1572
Gruenwald, R. B., & Viegas-Aldrovandi, S. M. 1987, A&AS, 70, 143
Guessoum, N., & Gould, R. J. 1989, ApJ, 345, 356
Guide Star Catalog. 1989 (Baltimore: STScI), CD-ROM
Haschick, A. D., & Baan, W. A. 1985, Nature, 314, 144
Haschick, A. D., Baan, W. A., Schneps, M. H., Reid, M. J., Moran, J. M., & Gusten, R. 1990, ApJ, 356, 149
Heckman, T. M. 1980, A&A, 87, 152
Heckman, T. M., Armus, L., & Miley, G. K. 1990, ApJS, 74, 833 (HAM)
Heiles, C. 1990, ApJ, 354, 483
Henkel, C., Güsten, R., Downes, D., Thum, C., Wilson, T. L., & Biermann, P. 1984, A&A, 141, L1
Hummel, E., van der Hulst, J. M., & Dickey, J. M. 1984, A&A, 134, 207
Hummel, E., van Gorkom, J. H., & Kotanyi, C. G. 1983, ApJ, 267, L5
Hunter, D. A., et al. 1986, ApJ, 303, 171
Innes, D. E. 1992, A&A, 256, 660
Irwin, J. A., & Seaquist, E. R. 1988, ApJ, 335, 658
———. 1991, ApJ, 271, 111
Irwin, J. A., Seaquist, E. R., Taylor, A. R., & Duric, N. 1987, ApJ, 313, L91
Irwin, J. A., & Sofue, Y. 1992, ApJ, 396, L75
Keel, W. 1983, ApJ, 269, 466
Koo, B.-C., & McKee, C. F. 1990, ApJ, 354, 483
———. 1992a, ApJ, 388, 93
———. 1992b, ApJ, 388, 103
Lawrence, A., Ward, M., Elvis, M., Fabbiano, G., Willner, S. P., Carleton, N. P., & Longmore, A. 1985, ApJ, 291, 117
Mac Low, M.-M., & McCray, R. 1988, ApJ, 324, 776 (MM)
Mac Low, M.-M., McCray, R., & Norman, M. L. 1989, ApJ, 337, 141 (MMN)
Maeder, A. 1990, in Massive Stars and Starburst Galaxies, ed. C. Leitherer, N. R. Walborn, T. M. Heckman, & C. A. Norman (Cambridge: Cambridge Univ. Press), 97
Mathis, J. S. 1990, ARAA, 28, 37
McCall, M. L., Rybski, P. M., & Shields, G. A. 1985, ApJS, 57, 1
McCarthy, P. J., Heckman, T. M., & van Breugel, W. 1987, AJ, 92, 264
McCray, R., & Kafatos, M. 1987, ApJ, 317, 190
Mineshige, S., Shibata, K., & Shapiro, P. 1993, ApJ, 409, 663
Norman, C. A., & Ikeuchi, S. 1989, ApJ, 345, 372
Oke, J. B., & Gunn, J. E. 1982, PASP, 94, 586
———. 1983, ApJ, 266, 713
Osterbrock, D. E., & Martel, A. 1992, PASP, 104, 76
Ostriker, J. P., & McKee, C. F. 1988, Rev. Mod. Phys., 60, 1

Palous, J., Franco, J., & Tenorio-Tagle, G. 1990, A&A, 227, 175
Péquignot, D. 1984, A&A, 131, 159
Reichert, G. A., Mushotzky, R. F., & Filippenko, A. V. 1994, in Mass-Transfer Induced Activity in Galaxies, in press
Rieke, G. H., et al. 1980, ApJ, 238, 24
———. 1985, ApJ, 290, 116
Salpeter, E. 1955, ApJ, 121, 161
Schiano, A. V. R. 1985, ApJ, 299, 24
Scoville, N. Z., & Good, J. 1986, in Star Formation in Galaxies, ed. C. J. Lonsdale Persson (NASA Conf. Publ. 2466), 3
Seaquist, E. F., Davis, L. E., & Bignell, R. C. 1978, A&A, 63, 199
Shields, J. C. 1992, ApJ, 399, L27
Shull, J. M., & McKee, C. F. 1979, ApJ, 227, 131
Slavin, J. D., & Cox, D. P. 1992, ApJ, 392, 131
Slavin, J. D., Shull, J. M., & Begelman, M. C. 1993, ApJ, 407, 83
Smith, S. J., Kennel, C. F., & Coroniti, F. V. 1993, ApJ, 411, 581
Sofue, Y., & Irwin, J. A. 1992, PASJ, 44, 353
Soifer, B. T., et al. 1987, ApJ, 320, 238
Stasińska, G. 1984, A&A, 135, 341
Stauffer, J. R. 1982, ApJ, 262, 66
Stone, R. P. S. 1977, ApJ, 218, 767
Taylor, D., Dyson, J. E., & Axon, D. J. 1992, MNRAS, 255, 351
Tenorio-Tagle, G., & Bodenheimer, P. 1988, ARAA, 26, 145
Tenorio-Tagle, G., Bodenheimer, P., & Rózyczka, M. 1987, A&A, 182, 120
Tenorio-Tagle, G., & Palous, J. 1987, A&A, 186, 287
Terlevich, R. 1992, in Relationships between Active Galactic Nuclei and Starburst Galaxies, ed. A. V. Filippenko (San Francisco: ASP), 133
Terlevich, R., & Melnick, J. 1985, MNRAS, 213, 831
Tilanus, R. P. J., & Veilleux, S. 1994, in preparation
Tomisaka, K. 1990, ApJ, 361, L5
Tomisaka, K., & Ikeuchi, S. 1988, ApJ, 330, 695 (TI)
Tully, R. B., Shaya, E. J., & Pierce, M. J. 1992, ApJS, 80, 479
Turnshek, D. 1988, in Quasar Absorption Lines: Probing the Universe, ed. C. Blades, D. Turnshek, & C. Norman (Cambridge: Cambridge Univ. Press), 17
Veilleux, S., Bland-Hawthorn, J., Cecil, G., & Tully, R. B. 1994a, ApJ, submitted (Paper II)
Veilleux, S., Bland-Hawthorn, J., Tully, R. B., & Cecil, G. 1990, BAAS, 22, 1315
Veilleux, S., Kim, D.-C., Sanders, D. B., Mazzarella, J. M., & Soifer, B. T. 1994b, ApJ, submitted
Veilleux, S., & Osterbrock, D. E. 1987, ApJS, 63, 295 (VO87)
Veilleux, S., Tully, R. B., & Bland-Hawthorn, J. 1993, AJ, 105, 1318
Viegas-Aldrovandi, S. M., & Contini, M. 1989, ApJ, 339, 689
Viegas-Aldrovandi, S. M., & Gruenwald, R. B. 1988, ApJ, 324, 683
Weaver, R., et al. 1977, ApJ, 218, 377
Weiler, K. W., Sramek, R. A., van der Hulst, J. M., & Panagia, N. 1983, in IAU Symp. 101, Supernova Remnants and Their X-ray Emission, ed. J. Danziger & P. Gorenstein (Dordrecht: Reidel), 171
Weymann, R. J., Scott, J. S., Schiano, A. V. R., & Christiansen, W. A. 1982, ApJS, 262, 497
Willner, S. P., Elvis, M., Fabbiano, G., Lawrence, A., & Ward, M. J. 1985, ApJ, 299, 443
Young, J. S., Claussen, M. J., & Scoville, N. Z. 1988, ApJ, 324, 115